Concluding Report: Quantitative Tomography Simulations and Reconstruction Algorithms

M. B. Aufderheide III, H. E. Martz Jr., D. M. Slone, J. A. Jackson, A. E. Schach von Wittenau, D. M. Goodman, C. M. Logan, J. M. Hall

February 1, 2002

U.S. Department of Energy

Lawrence
Livermore
National
Laboratory

DISCLAIMER

Concluding Report:　Quantitative Tomography Simulations and Reconstruction Algorithms

Maurice B. Aufderheide III, Harry E. Martz Jr., Dale M. Slone, Jessie A. Jackson, Alexis E. Schach von Wittenau, Dennis M. Goodman, Clinton M. Logan, and James M. Hall

Lawrence Livermore National Laboratory

Abstract. In this report we describe the original goals and final achievements of this Laboratory Directed Research and Development project. The Quantitative was Tomography Simulations and Reconstruction Algorithms project (99-ERD-015) funded as a multi-directorate, three-year effort to advance the state of the art in radiographic simulation and tomographic reconstruction by improving simulation and including this simulation in the tomographic reconstruction process. Goals were to improve the accuracy of radiographic simulation, and to couple advanced radiographic simulation tools with a robust, many-variable optimization algorithm. In this project, we were able to demonstrate accuracy in X-Ray simulation at the 2% level, which is an improvement of roughly a factor of 5 in accuracy, and we have successfully coupled our simulation tools with the CCG (Constrained Conjugate Gradient) optimization algorithm, allowing reconstructions that include spectral effects and blurring in the reconstructions. Another result of the project was the assembly of a low-scatter X-Ray imaging facility for use in nondestructive evaluation applications. We conclude with a discussion of future work.

1.　MOTIVATION

Radiography is the process of inferring the properties of an object by examining the shadow (a projection) formed by some form of penetrating radiation, such as X-Rays, neutrons, or protons. Tomography is the process of reconstructing an absorption map of the object from a set of radiographic projections. This absorption map is related in some way to the original density distribution and elemental composition of the object, but this relationship is often complex. These techniques are typically used when one needs to see deep inside an object, which has a complex structure that obscures optical or sonic investigation. These techniques are used in a variety of industries for quality control and nondestructive evaluation. At LLNL, these techniques are used for nondestructive evaluation applications and as diagnostics for the National Nuclear Security Agency's (NNSA's) dynamic experiments in Inertial Confinement Fusion (ICF), the National Ignition Facility (NIF), and the Stockpile Stewardship Program and Advanced Radiography Campaign.

A long-term goal of the Advanced Radiography Campaign is to be able to reconstruct object densities with roughly 1% accuracy for images with fairly large fields of view and large optical depths. Achieving this accuracy will require excellent understanding and control of the sources of systematic error in tomography. Most current tomographic algorithms provide reconstructions of objects that can be trusted qualitatively, or used for locating defects and interfaces within an object, but they do not provide accurate density mappings. In fact, the currently used algorithms in tomography, such as filtered back-projection[1], return maps that are the product of density and an effective mass absorption coefficient. A major reason for these inadequacies is that such traditional algorithms make very drastic simplifying assumptions

about the physics of radiography. This discussion is continued in the second section of this report.

There were two main goals in this project: 1. to improve our ability to simulate radiography to get as close to 1% accuracy as possible, and 2. to improve the accuracy of tomographic reconstruction by including the physics of radiography in the reconstruction process. To achieve the first goal, the project sought to improve the HADES radiographic simulation code[2]. This code simulates radiography using ray-tracing techniques. As will be discussed below, ray-tracing techniques are much faster than Monte-Carlo transport techniques and are thus more amenable for coupling with tomography codes, but they are less accurate than Monte-Carlo. We used more complete Monte-Carlo transport techniques to help build physically accurate models for spectra and detector response in HADES. We will describe this approach in the third section of this report. To improve our tomographic accuracy, we have gone back to the full, non-linear equation that governs X-Ray radiography and have developed an algorithm that optimizes this system. We use the newly validated HADES code to do the needed forward- and back-projections in the optimization cycle. We will describe this approach in the fourth section of the report.

In the fifth section of the report, we describe other results of this project. We conclude in the final section with a discussion of remaining research areas.

2. FUNDAMENTAL EQUATIONS OF RADIOGRAPHY AND TOMOGRAPHY

Consider an X-ray source, an imaging detector, and an object between the source and detector. For X-rays passing through the object, the attenuation along ray i can be expressed most generally by

$$y_i = \frac{I}{I_o} = \sum_j B_{ij} B'_{ij} \left[S_j \exp\left(-\sum_l \sum_k \boldsymbol{m}_{ljk} a_{ik} x_k \right) + \boldsymbol{z}_j \right] \tag{1}$$

where I and I_o are the transmitted and incident X-Ray intensity, B_{ij} and B'_{ij} are energy-dependent blur matrices due to detector blur and spot blur convolved at the detector plane, S_j is the incident dose or number of photons (depending on the sort of detector used) in energy bin j, μ_{ljk} is the mass absorption coefficient of material l in voxel k at energy bin j, a_{ik} are the ik^{th} elements of the geometry matrix A, which relates the path length along ray i through voxel k, x_k is the object density in voxel k, and ζ_j is the scattered radiation reaching detector pixel i. The summation over j corresponds to integration over X-Ray energies, while the summation over l corresponds to integration over materials, and the summation over k ranges over all voxels through which ray i passes. Implicit in equation (1) is the dependence on the blur functions, B, on neighboring pixels (*i.e.* neighboring values of i). Also implicit in equation (1) is the dependence of the scatter field, ζ, on the X-Ray source, object characteristics, and experimental geometry.

If some rather drastic simplifying assumptions are made, equation (1) can take a much simpler form. In the case of no blur, no scatter, a single material, and a monochromatic X-Ray source, equation (1) takes the form:

$$y_i = \frac{I}{I_o} = \exp\left(-\sum_k \boldsymbol{m}_k a_{ik} x_k \right) \tag{2}$$

and this equation can be recast as

$$y'_i = -\ln\left(\frac{I}{I_o}\right) = \sum_k \boldsymbol{m}_k a_{ik} x_k \tag{3}$$

It can be seen that equation (3) is much more tractable than equation (1) because there is a linear relationship between x and y'. Equation (3) is the standard starting point for most work in both active and passive tomography, because of its simple relation between the (logarithm of) projections and line integrals through the object. While equation (3) is very amenable to a variety of solution strategies, it is a drastic simplification of the true physics in radiography. In the case of traditional medical tomography and radiography, this simple formulation has been adequate for a number of reasons. First, in most commercial systems, highly collimated X-ray beams are used, reducing the scatter field and the effects of blur. Second, because biological objects are mainly bags of water, with relatively small changes in mass absorption coefficients (and density) among various biological materials, spectral effects are not overwhelming and can be handled phenomenologically. Third, the goal of much of medical radiography and tomography is imaging, not quantitation, so absolute density values are not relevant, as long as the clinician can see the tissues of interest.

Radiography and tomography in LLNL applications are typically very different from medical applications for a number of reasons. First, LLNL applications require a wide variety of probes: X-Rays with energies ranging from a few keV to 100 MeV, neutrons with energies ranging from thermal to 800 MeV, and protons with energies ranging from 800 MeV to 100 GeV. We do not have time to develop a phenomenology for each case. Second, lab applications, and industrial applications in general, examine objects that have a much larger variation in size and composition than medical subjects. In particular, we are concerned with objects composed of dense metals, plastics, air, and even high explosives. This requires the use of higher energy probes than in medicine, and a greater concern about spectral effects. Third, at the Lab, we frequently must use a wide two-dimensional field of view, rather than fan or pencil beams. Also, the number of views may be quite limited due to the dynamic nature of the object, or difficulties in viewing the object from particular angles. These differences necessitate the more rigorous and general approach that was the subject of our research.

3.   VALIDATING RADIOGRAPHIC TECHNIQUES

The user has two main options in performing radiographic simulation: Monte Carlo techniques, and ray-tracing techniques. Monte Carlo techniques allow the user to study the "full" physics of radiography using many simulation particles to interact with the object, including source generation and detector properties. In principle, this approach allows the user to include all the relevant processes for radiography: absorption, scattering, and secondary particle production. For X-Rays some Monte Carlo codes with all or some of this capability are MCNP[3], COG[4], TART[5], the integrated Tiger series[6], and EGS4[7]. Unfortunately, these codes are very slow and cumbersome in the simulation of radiographic images. For a 300x300 image with 1% Monte Carlo statistical fluctuations, at least 10^9 particles must be transported through the system, which, on current serial machines, requires roughly 2000 hours

of CPU time. While this is becoming feasible with modern massively parallel machines, such capability is not available for routine studies of radiography.

Ray-tracing techniques are very useful for studies requiring a fast turnaround time. In this approach, a bundle of rays connecting the radiographic source and detector is traced through the specified system. The total path length along each ray is computed and stored in each pixel of the simulated detector. Spectral effects, various instrumental blurs and dose conversion can be included in the calculation. Since the path length computation only occurs along each straight ray, scattering effects are not computed with such a code, although they can be included after the fact. Because of the greater simplicity of this technique, ray-tracing simulations are much faster than their Monte Carlo cousins and can be performed on workstations or fast PCs or Macs. XRSIM[8], SINDBAD[9] and HADES[2] are examples of ray tracing radiographic simulation codes.

HADES is a ray-tracing code that we have been developing for the simulation of radiography used in industrial NDE settings. The name HADES was derived from Greek mythology. For HADES, the fundamental object description is a meshed model of an object. By "mesh", we do not mean the surface meshes often discussed in computer graphics[10,11], but rather a finite-element or finite-difference mesh, which describes the volume of the object. HADES can radiograph 2D r-z meshes of varying types, as well as 3D meshes of complexity ranging from Cartesian meshes to unstructured generalized hexahedral meshes. This ability to trace through meshes is relatively unique in HADES as a radiography code and has enabled us to couple to optimization algorithms for doing reconstructions into a mesh. For coupling to tomography, we have thus far used 3D Cartesian meshes.

HADES also has a library of solid-body objects such as plates, spheres, cones, cylinders and other complex shapes that can be included in a simulation. Recently we have added constructive solid geometry operations such as intersections, unions and differences to allow more complex objects to be built and radiographed. HADES can even run without any mesh, only using combinations of solid body objects.

Because of the wide variety of radiographic probes used in Livermore projects, we have given HADES the capability to support these probes. HADES can simulate X-Ray radiography for photon energies ranging from roughly ~1 keV to 100 MeV. Spectral and monochromatic sources can be simulated by the code. HADES uses the Livermore Evaluated Photon Data Library[12] for X-Ray absorption cross-sections. HADES can also simulate neutron radiography for neutron energies ranging from roughly thermal energies up to 30 MeV. HADES uses the Livermore Evaluated Neutron Data Library[13] for these simulations. Again, the user can specify spectral or monochromatic neutron sources. HADES can also simulate high-energy proton radiography for proton energies ranging from ~800 MeV up to ~100 GeV, taking into account Gaussian multiple Coulomb scattering. For this work, HADES uses the Letaw nuclear attenuation cross-sections[14] and Dahl's expression for radiation length[15]. This coupling of the code to accurate cross-section data sets is another essential element in doing quantitative radiographic simulations or tomographic reconstructions. More information about HADES can be obtained in reference [2] and also in reference [16].

HADES models the spectral character of sources and detectors in a straightforward fashion. The user specifies the source spectrum over a set of energy bins, as well as the dose of the source, in units of Roentgen at 1 meter. HADES computes a path length image for each energy bin. A detector file is also input to HADES that specifies the radial blur function of the detector as a function of incident X-ray energy. Another input file provides the total energy deposit and

detector quantum efficiency (DQE) of the detector as a function of incident X-Ray energy. Using the path length image at each energy bin, HADES combines all of this information into a radiographic image, properly blurred and summed together, as specified by the detector files. The source and detector files require knowledge of the radiographic system that can only be calculated at present with Monte-Carlo codes. This approach allows HADES to use the full physics of Monte-Carlo, without requiring heroic amounts of computer time for each simulation. Schach von Wittenau discusses this approach in more detail in a paper prepared during this project, which is the first appendix to this report[17].

For these validation studies, we have chosen a Varian Linatron 3000 operating at nominally 9 MeV as our X-Ray source. We have used a variety of large format amorphous silicon arrays as our imaging detectors.

Early in the project[18], we used MinR scintillator screens plus dpiχ large format amorphous silicon arrays. We used a 14 step copper step wedge to test our ability to simulate the correct amount of attenuation in the system. The step thicknesses in the system vary from roughly 0.34 cm to 10.2 cm. Because of the large size of the object relative to the imaging array, relatively low magnifications were used. Magnifications ranged from nearly 1 to 1.2. The source to detector distance was 6 m. In Figure 1, we display the step wedge and its experimental radiograph, when magnification was 1.2.

In this figure, we also show a lineout across the step wedge and compare it with two HADES simulations. In the first comparison, HADES included the 9 MeV bremsstrahlung spectrum in its simulation, but the detector response was not modeled. In the second comparison, the bremsstrahlung spectrum and energy-dependent blur of the dpiχ detector was included in the simulation. The second simulation shows better agreement to the blurring seen in the radiograph. Agreement between simulation and experiment was at the 3% level, but the scattered background was treated as a uniform value that was determined by optimizing the fit to the data.

A year later, this experiment was revisited with a number of new features[17]. A set of lead collimators was built so that the object and detector would be shielded from excessive amounts of scattered and direct radiation. An improved detector (a Varian Flashscan 4030, fitted with a Kodak Lanex-Fine scintillating screen) was used. Also, a different set of copper step wedges was used. These step wedges produced a smaller, more symmetric, scatter profile.

Figure 2 shows some results from this recent experiment. Two step wedges of identical height profiles, but differing widths, were radiographed. The widths were varied to test how well HADES and its Monte-Carlo generated blur models were able to simulate the actual blurring over a variety of contrasts and length scales. The lineouts demonstrate that even better agreement was achieved in the new experiment. It should also be emphasized that in this experiment, no arbitrary scatter background was necessary for fitting the wedges. The HADES simulation is now agreeing with data at the 2% level. These results were an improvement over the first experiment for several reasons. First, the collimation in the new system drastically reduced the scatter background in the system. Second, HADES had a more accurate model of the new detector. Third, the new detector was more reliable than the imager originally used. More discussion of this experiment is given in Appendix 1 of this report[17].

These results have validated HADES simulation techniques at the 2% level. We are aiming for 1% agreement, but this current agreement is 5 to 10 times better than the 10% to 20% agreement obtained in the past. These results are also important because they demonstrate that a full-up Monte-Carlo simulation is not necessary for simulating every radiograph, as long as

more detailed and accurate calculations are used in the ray-traced simulations of the source and detectors. In attempting to reach 1%, many complications arise. The cross sections used in HADES and Monte-Carlo simulations are only accurate at the few % level[12]. At MeV energies physical processes such as photonuclear absorption[19,20] and Delbrück scattering[21], which are not included in current tabulations, contribute at the 1% to 10% level. It is difficult to obtain completely accurate models for source and detector properties because they are trade secrets. Also, at this level of accuracy, X-Ray scatter off the air in the line of sight may need to be considered.

4. NONLINEAR TOMOGRAPHY

As noted in the second section, the equation that governs radiography for polychromatic sources and multiple materials is nonlinear. Equation (1) expresses this dependence. Radiography is the process of computing the projections y, given a model for the object x and the properties of the radiographic system (source spectrum and spot size, detector properties). Tomography is the process of reconstructing the object density x, given a set of projections y. The general problem of reconstructing the object *and* the radiographic system is too ill-posed to be solved for our kind of radiography. In this discussion, we assume we know the properties of the radiographic system. This is not a trivial statement, because radiographic images are integral objects and it is difficult to probe individual properties of the system. This is why validation studies of the type described in the previous section are needed.

In the results described below we have assumed that ζ, the scattering profile, can be ignored or reliably subtracted off. We also neglect the blur functions for now. Our radiographic equation then becomes:

$$y_i = \frac{I}{I_o} = \sum_j S_j \exp\left(-\sum_l \sum_k \boldsymbol{m}_{ljk} a_{ik} x_k \right) \tag{4}$$

where all terms have been defined in the Section 2. This is the same expression as equation (1), except that the blur terms B have become delta functions and ζ has been set to zero.

The tomography algorithm we seek would be best if, in the process of reconstruction, it also assigned materials as well as densities to each voxel. We have found that this problem, even with total knowledge of the radiographic system, is still too ill-posed to allow a unique solution. This fact is fairly easy to anticipate. In standard radiographic imaging, the spectral dependence is collapsed at the detector into a complex dot product, which yields a dose or intensity value for each pixel. While this spectral information could, in principle, give hints about which materials are present, the information has mostly been lost in the detector measurement. Thus, if one allows the μ and the x values both to be free, they can compensate for one another, yielding a continuum of solutions.

In order to solve this difficulty, we have further constrained the nature of the reconstruction by stipulating that the user supplies a model of the object that assigns a material to each voxel. The code uses this model to assign μ values for all voxels, allowing a reconstruction in only x to take place. It is fair to ask how realistic such a requirement is, since the whole point of tomography is to determine this structure.

For the applications we envision (industrial and laboratory applications), the user does know the materials that constitute the object, but not necessarily their location in the object at

radiograph time. It is expected that, using the radiographic projections, the user will do a rough reconstruction first using one material only. This reconstruction will show sharp gradients in the effective density, which can be used to assign the correct location of each material. The full reconstruction can then be done using the correct material assignments. This process could be repeated as the density model of the object becomes more refined. This process could even be automated, although it has not in this project.

The general approach we have taken to the tomography problem is shown in Figure 3. The measured projections of the object are compared with the simulated projections of a trial object. This comparison is done in a cost function, which weights the differences based on the statistical properties of the detection system. A minimizer algorithm then uses these weighted differences to modify the object, seeking a better match between projections. This new object is then fed back into the simulator, beginning a new iteration of the algorithm.

In this project, we have used HADES for simulating radiographs. The minimization algorithm we have used is the CCG (Constrained Conjugate Gradient) algorithm, developed by Goodman *et al.*[24,25]. This algorithm is designed to search for extrema in spaces with a large number of dimensions using conjugate gradients[22,23] to determine the search direction. This algorithm is special in that it only allows extremization within user specified constraints. It has already been used successfully in image deconvolution[24] and passive computed tomography[25,26].

CCG requires the use of some estimate for the first and second derivatives of the system of interest. These estimates involve the back projection of the geometry matrix operating on various entities. A major area of effort in the project has been developing code so that HADES could do these back projections. Since HADES started as strictly a radiographic simulation code (forward projections), this has involved making HADES run "backwards" to some extent.

In Table 1 we have summarized the formulas used in the full non-linear case described in Equation 1. We have also shown the analogous equations for the linear, single-material case. In these expressions, we have retained the blur and scattering terms for completeness, but they are not included in the current algorithm. In these expressions, wherever the transpose occurs, a back projection is needed. Figures 4a and 4b show the flow of the coupled code. Whenever CCG needs forward- or back-projections of quantities, they are passed to HADES, which does the needed projection. CCG and HADES operate concurrently as separate processes, passing information to one another using files. In this way, we avoided the complications of mixing two very different codes at the binary level.

In the process of developing HADES-CCG, a number of other codes were also developed. The linear tomography code is LCONE-CCG. A prototype nonlinear code, called MCONE-CCG was also developed. MCONE-CCG and HADES-CCG produced numerically identical results, but MCONE-CCG does not have access to the atomic physics data that HADES provides. In running MCONE-CCG, spectrally dependent mass absorption coefficients, obtained from HADES, had to be input to the code before execution.

As mentioned above, one of the advances achieved with MCONE-CCG and HADES-CCG was the inclusion of mass absorption coefficients explicitly in the algorithm. Because of this inclusion, MCONE-CCG and HADES-CCG reconstruct a model of the object in units of density, not the product of density and mass absorption coefficient. Also, the materials within the object have already been assigned as an initial condition. However, this definition also leads to some additional complication, because some of the operations in the reconstruction (see Figure 4) require that the codes keep track of the images for each material at each energy group. If there are l materials and j energy groups, this means that lxj images must be stored as

the code iterates. This is a much larger memory requirement than in the case of traditional tomographic algorithms, such as filtered back projection.   This is particularly worrisome when one remembers that tomography requires images at some number of angles, further increasing the memory requirements. This need for large amounts of memory has challenged the code when dealing with large data sets.

Nevertheless, this approach has shown some promising results. As a first example, consider a cylinder of one material of uniform density, radiographed with a notional flat, 40-bin, X-ray spectrum ranging from 0 to 9 MeV. The cylinder material was given a density of 0.001 g/mm^3 and the spectral dependence of the mass absorption coefficients was defined so that the lowest five energy bins had values of 10 mm^2/g and all higher bins had values of 1 mm^2/g. This object was radiographed and reconstructed with LCONE-CCG and MCONE-CCG and the density profiles are displayed in Figure 5. The linear result has been divided by an effective mass absorption coefficient, so that its reconstruction can be expressed as a density for comparison with the nonlinear case. It can be seen that the linear case exhibits a nonphysical increase in density from the center outward. This is the result of spectral hardening in the object and it is gratifying that the nonlinear case reconstructs this correctly as was argued above.

We next consider the case of a cylindrical object composed of one material with two densities. The outer cylindrical shell has a density of 0.003 g/mm^3, while the inner core has a density of 0.001 g/mm^3. The details of the spectrum and mass absorption coefficients are the same as in the first example. Figure 6 shows the density profiles for this case. Again, the MCONE-CCG computes the density correctly, without the presence of spectral hardening artifacts.

For the next example, we use an X-Ray spectrum characteristic of the Linatron 3000 Linac (9 MeV Bremsstrahlung) and consider a cylinder composed of aluminum with the appropriate mass absorption coefficients for aluminum. The density profiles, as shown in Figure 7, exhibit the same features as the previous two cases: MCONE-CCG can successfully return the density profile, while LCONE-CCG exhibits spectral hardening effects. One difference between this case and those previous is that the "cupping" of the linear density profile is less pronounced. This can be understood if one considers the interaction of the bremsstrahlung spectrum with the energy dependence of the mass absorption coefficients. The part of the spectrum that penetrates the object the most will be gamma rays in the 1-6 MeV energy range. Lower energy photons are strongly depleted by the photoelectric effect, while bremsstrahlung produces few photons above this range. Within the 1-6 MeV energy range, photon attenuation is dominated by Compton scattering, which has relatively small variation with energy. Thus, there is less spectral hardening seen in the linear reconstruction.

The last study was a cylindrical object composed of an outer shell of aluminum, an inner shell of lead, and an inner core of plastic. This object was radiographed with the Linatron 3000 source and imaged with the Varian Flashscan 4030. For the full data set, over 590 angles were used.   In this study a smaller subset was used.   The data were then reconstructed using convolution back projection, LCONE-CCG, and MCONE-CCG. The results are shown in Figure 8. It can be seen that the linear approach produces a similar density profile to the convolution back projection (CBP) algorithm, except that the CBP algorithm is much noisier. This difference is a result of CBP's poor response to noisy data and the linear algorithm's forming a least-squares fit to the data. Both sets of data exhibit significant deviations from the actual density profile. The nonlinear reconstruction shares the good noise handling properties of the linear method and also is getting closer to the actual density profile.

It is disappointing that the nonlinear result is not in better agreement with the actual density profile, but not surprising. In this reconstruction, we did not include the actual spectral sensitivity of the detector, because this was our first effort with real data. Also, we have not included every bit of attenuation in the field of view. The source model is that of a bare source. More detail probably needs to be included in this source model. Scattering may also be contributing systematic errors to the reconstructions. These details will have to be examined in future work.

This sensitivity to the radiographic details of the imaging system is to be expected. We have included a physically realistic model for radiography in the algorithm, and this detail is required if the algorithm is to produce meaningful answers. Such an approach to tomography and radiography is much more detailed than has been standard practice, but it is required if great quantitative accuracy is wanted for the application.

5.   OTHER RESULTS OF THIS PROJECT

In the process of attempting to perform high precision radiography, it was found that the scatter background in the Building 239 radiography facility was unacceptably high. A number of MCNP studies were done by Alexis Schach von Wittenau to design collimation that would reduce this background. These studies were done as part of this project and resulted in the design of the Stonehenge assembly of collimators. The cost of fabricating and installing the system was not paid for by this project. An image of these collimators is shown in Figure 9. This project thus resulted in an improvement to the infrastructure of the LLNL nondestructive evaluation program. In addition, this design was later used as a baseline for studies to design an improved radiography facility for Pantex Bay 19. A report on these studies is given in Appendix 2.

As was described in the section 3, HADES was improved through the introduction of more accurate detector models. But HADES has also benefited in two other ways from this project. First, the scope of the code was broadened. Originally HADES was designed to simulate a radiograph from a single view. As part of this project, HADES was generalized to compute radiographs for an ensemble of views. Second, in the process of sharing HADES with users in Engineering, HADES underwent a code Review and Release (UCRL-CODE-99035). In addition, a record of invention for the code was submitted and the lab decided that HADES did not merit pursuit of a patent. Similarly, a record of invention for HADES-CCG was submitted and the lab decided that HADES-CCG did not merit pursuit of a patent. These actions have allowed us to communicate more freely and eventually collaborate with colleagues outside the lab.

Another benefit of this project was the multidisciplinary team that resulted. This effort required the efforts of specialists in the area of radiographic simulation (Aufderheide, Slone, and Schach von Wittenau), radiographic analysis (Martz, Logan, Aufderheide, and Schach von Wittenau), computer science (Jackson and Slone), and experts in the CCG optimization code (Goodman and Jackson). Personnel from four directorates (Defense and Nuclear Technologies, Engineering, Computations, and Physics and Applied Technology) worked on this project. In the process of doing the work, we learned each other's formats and developed some common standards. This greater level of communication will allow more efficient work in the future.

6. FUTURE WORK

Great progress has been made toward our goal of high precision radiography and tomography. We have demonstrated 2% accuracy in radiographic simulation. We have constructed a nonlinear tomography code that has demonstrated significant improvement over the current state of the art. But many issues have also arisen in the work, which will have to be addressed in future work.

First, we have seen that more work needs to be done to fully characterize radiography and tomography systems. Details needed for accurate work include: an accurate specification of the source materials, geometry, intensity, and energy; a complete description of all nuisance or shielding materials in or near the field of view, even if flat plates; a complete description of the detection medium, so that it can be modeled in HADES. Current standard practice in industrial tomography is very cavalier about this information.

We need to apply these techniques to more systems, in order to detect bugs, errors in our reasoning, and needed code refinements. There are many ongoing experiments to which these tools will be applied.

In the process of merging HADES and CCG, we found that we were pushing HADES well beyond the paradigm it was designed to handle. In addition there are a number of future applications, such as radiography of radioactive objects (waste drums), NIF backlighting experiments, various pinhole imaging applications, and the need to simulate some aspects of scatter, which are leading us to consider a rewrite of HADES. What is needed is a more object-oriented approach to the casting of rays and transmitting energy through objects.

HADES-CCG is only a prototype code and much needs to be done to improve its operation. First, some streamlining is needed in order to allow the codes to communicate better together. Second, it would be useful to have the code running on more platforms than just SGI workstations. Third, some work needs to be done in order to speed up the operation of the code by either reducing its footprint or parallelizing it, or both.

In most of the topics discussed in this report, the scattering of X-rays has been a problem. Our group went to great effort to reduce scatter in our Linatron experiments, but it is still present. For many of our applications, it is unlikely that we will be able to eliminate scatter. We will thus have to develop a better understanding of scatter and learn how to correct for it.

7. ACKNOWLEDGMENTS

8. REFERENCES

1. Kak, A. C., and Slaney, M., *Principles of Computerized Tomographic Imaging*, IEEE Press, New York, 1988.
2. Aufderheide, M. B., Slone, D. M., and Schach von Wittenau, A. E., *HADES, A Radiographic Simulation Code*, in Review of Progress in Quantitative Nondestructive Evaluation, Vol. 20A, 2000, AIP Conference Proceedings 557, p 507-513.
3. MCNP4C User's Manual, available through the Radiation Safety Information Computational Center (RSICC). Available online at
http://www-rsicc.ornl.gov/ documents/pdf/ccc/ccc7/c700.pdf
4. Wilcox, T.P, and Lent, E.M., *COG User Manual*, UC Report Number M-221-1, 1989.
5. Cullen, D.E., *TART-96: A Coupled Neutron-Photon 3-D Combinatorial Geometry Monte Carlo Transport Code*, UC Report Number UCRL-ID-126455, 1996.
6. Halbleib, J.A., and Kensek, R.P., ITS Version 3.0: The Integrated TIGER Series of Coupled Electron/Photon Monte Carlo Transport Codes, Sandia Report SAND91-1634, 1992. Available online at
http://www-rsicc.ornl.gov/documents/pdf/ccc/ccc4/c467.pdf
7. Bielajew, A.F, Hirayama H., Nelson, W.R., and Rogers, D.W.O., History, Overview, and Recent Improvements of EGS4, National Research Council of Canada Report NRC-PIRS-0436, 1994. Available online at
http://www-rsicc.ornl.gov/documents/pdf/ccc/ccc3/c331.pdf
8. Xu, J., Wallingford, R.M., T. Jensen, and Gray, J.N., "Recent Developments in the X-Ray Radiography Simulation Code: XRSIM", in Review of Progress in Nondestructive Evaluation, 13A, (1994), pp. 557-562.
9. Glière, A., "SINDBAD: From CAD Model to Synthetic Radiographs", in Review of Progress in Nondestructive Evaluation, 17A, (1998), pp. 387-394.
10. Salomon, D., Computer Graphics and Geometric Modeling, Springer-Verlag, New York, 1999.
11. Fleming, B., 3D Modeling and Surfacing, Academic Press, San Francisco, 1999.
12. Cullen, D.E., et al., Tables And Graphs Of Photon-Interaction Cross Sections From 10 eV To 100 GeV Derived From The LLNL Evaluated Photon Data Library (EPDL), University of California Report Number UCRL-50400-Volume 6-Rev 4- Parts A & B, 1989.
13. Howerton, R.J., et al., The LLL Evaluated Nuclear Data Library (ENDL): Graphs of Cross Sections from the Library, University of California Report Number UCRL-50400-Volume 15-Part B, 1976.
14. Letaw, J.R., Silberberg, R., and Tsao, C.H., Ap.J. Supp., **51**, (1983) p. 271.
15. Dahl, O.I. as referenced in D.E. Groom et al., The European Physics Journal, **C15** (2000). Available online at http://pdg.lbl.gov/
16. Aufderheide, M. B., Slone, D. M., Schach von Wittenau, A. E., Ayers, J., and Mathews, A., *HADES User's Manual,* This document is in preparation but rough drafts can be provided to selected users.
17. Schach von Wittenau, A. E., Logan, C. M., Aufderheide, M. B., and Slone, D. M., *Blurring artifacts in megavoltage radiography with a flat-panel imaging system: Comparison of Monte Carlo simulations with measurements*, UCRL-JC-144247, submitted to *Medical Physics*.

18. Martz, H. E., Aufderheide, M. B., Goodman, D. M., Schach von Wittenau, A. E., Logan, C. M., Hall, J. M., and Jackson, J. A., *Quantitative Tomography Simulations and Reconstruction Algorithms*, UCRL 53868-99, 2000.
19. Ahrens, J. et al., *Nucl. Phys.,* **A251**, 479 (1975).
20. Berman, B. L., and Fulz, S. C., *Rev. Modern Phys*., **47**, 713 (1975).
21. Ruhlhusen, P., et al., *Phys. Rev*., **C23**, 1375 (1981).
22. Shewchuk, J. R., *An Introduction to the Conjugate Gradient Method Without the Agonizing Pain*, available online at http://www-2.cs.cmu.edu/~jrs/jrspapers.html.
23. Press, W. H., Teukolsky, S. A., Vetterling, W. T., and Flannery, B. P., Numerical Recipes in C 2nd Edition, Cambridge University Press, Cambridge, 1999.
24. Goodman, D. M., Johansson, E. M., and Lawrance, T. W., On Applying the Conjugate-Gradient Algorithm to Image Processing Problems, in Multivariate Analysis: Future Directions, ed. by C. R. Rao, Elsevier Science Publishers B.V., (1993), 209-232.
25. Jackson, J. A., Goodman, D. M., Roberson, G. P., Martz, H. E., "An Active and Passive Computed Tomography Algorithm with a Constrained Conjugate Gradient Solution", in *Proceedings of the 6th Nondestructive Assay and Nondestructive Examination Wast Characterization Conference*, (1998) pp. 325-358, UCRL-JC-130818.
26. Goodman, D. M., *Maximum Likelihood Estimation with Poisson (Counting) Statistics for Waste Drum Inspection*, UCRL-ID-127361.

Figures
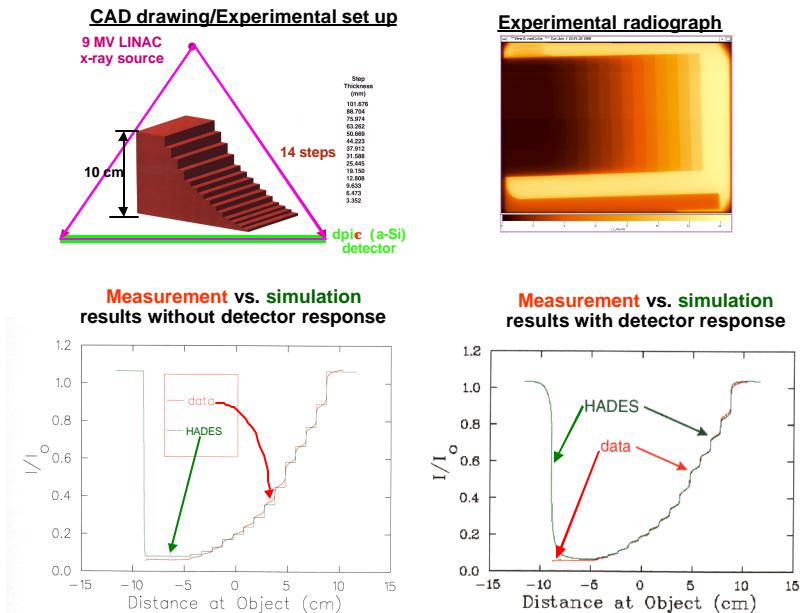
Figure 1: Using a copper step wedge to quantify HADES' simulation capabilities. The upper row shows the step wedge and its radiograph, while the bottom row shows lineouts across the center of the step wedge radiograph and the HADES simulation. The plot at the bottom left illustrates that a poor fit is obtained if detector response is not included, while the plot at the right shows how detector response improves the simulation's fit to the data.
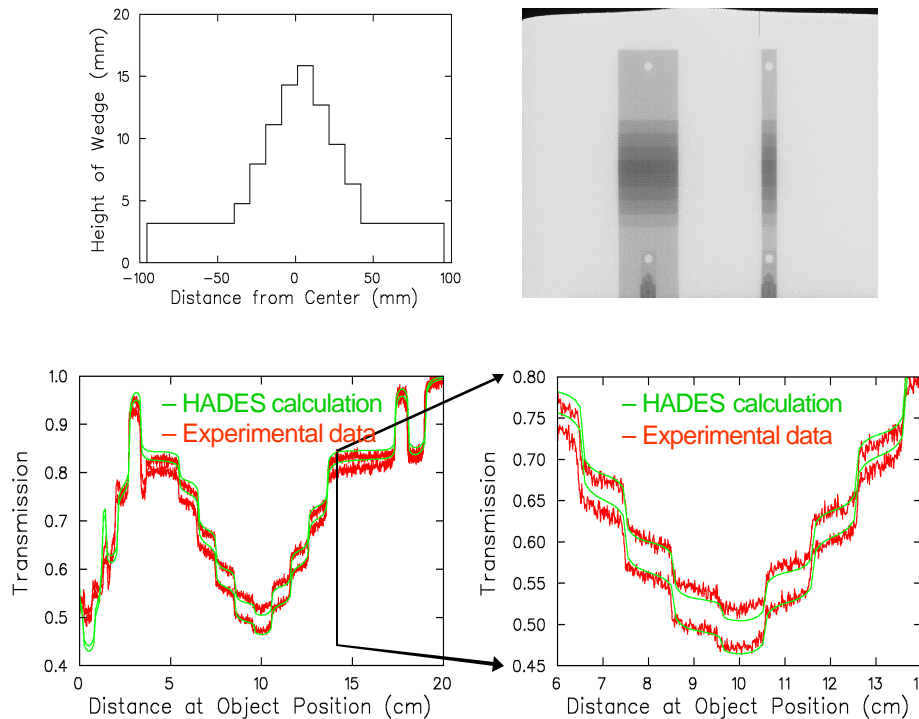
Figure 2: Results from most recent step wedge experiment. At upper left is a drawing of the new step wedges. At upper right is the radiograph analyzed. The wedge at left is 2.0" wide, while the wedge at right is 0.5" wide. The bottom row shows lineouts along the center of each wedge, compared with HADES simulations. The plot at right is an enlargement of the plot at left.
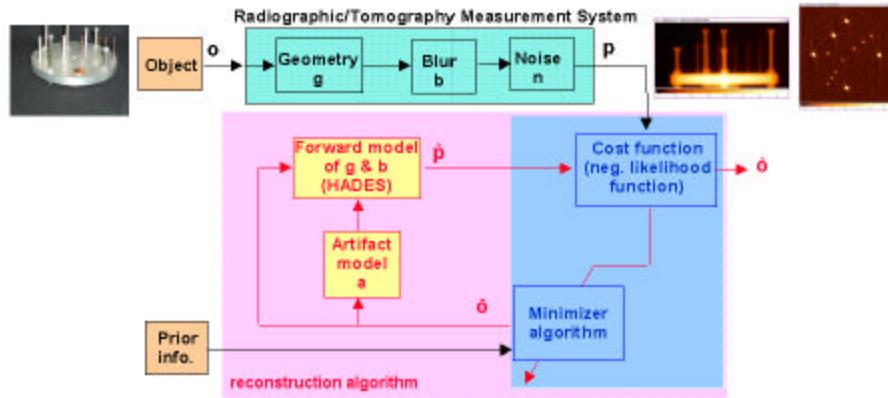
Figure 3: General Tomographic Approach. The object o is estimated by comparing its projections p with simulated projection $\hat{p}$, which was generated from an estimate of the object $\hat{o}$.

Table 1: Expressions for nonlinear and linear tomography.

	Multimaterial, non-linear	Single material, linear
Projection Signal	$y = I/I_o$	$y' = -\ln(I/I_o)$
Geometry Model	$\mathbf{w}^\circ = \mathbf{A}\hat{\mathbf{x}}^\circ$	$\mathbf{w}^\circ = \mathbf{A}\hat{\mathbf{x}}^\circ$
Absorption Model	$\hat{y}_i^\circ = \sum_j B'_{ij} B_{ij} S_j \left[\exp\left\{ -\sum_j \mu_{lj} w_l^{oi} \right\} - \zeta_{ij} \right]$	$\hat{y}_i^\circ = w_i^\circ$
Residual	$\Delta y_i^\circ = y_i - \hat{y}_i^\circ$	$\Delta y_i^\circ = y_i - \hat{y}_i^\circ$
Cost Function	$\text{fn}^\circ = \frac{1}{2}\sum_i \left(\Delta y_i^\circ\right)^2$	$\text{fn}^\circ = \frac{1}{2}\sum_i \left(\Delta y_i^\circ\right)^2$
Interium Value	$\left[r_m^\circ\right] = \Delta y_i^\circ \sum_j B'_{ij} B_{ij} S_j \mu_{mj} \exp\left\{ -\sum_l \mu_{lj} w_l^{oi} \right\}$	$r_i^\circ = \Delta y_i^\circ$
Approximate Gradient	$\mathbf{g}^t = -\mathbf{A}^{\mathbf{T}} \mathbf{r}^t$	$\mathbf{g}^t = -\mathbf{A}^{\mathbf{T}} \mathbf{r}^t$
Directional Derivative	$\text{dd}^t = \mathbf{g}^t \cdot \mathbf{d}^t$	$\text{dd}^t = \mathbf{g}^t \cdot \mathbf{d}^t$
2nd Directional Derivative	$\text{dd2}^t = \sum_m \sum_n \mathbf{v}_m^{\mathbf{T}} \mathbf{D}_{mn} \mathbf{v}_n$ where, $\quad \text{u}_1(i,m) = \sum_j B'_{ij} B_{ij} S_j \mu_{mj} \exp\left\{ -\sum_l \mu_{lj} w_l^i \right\}$ $\text{u}_2(i,m,n) = \sum_j B'_{ij} B_{ij} S_j \mu_{mj} \mu_{nj} \exp\left\{ -\sum_l \mu_{lj} w_l^i \right\}$ $\mathbf{D}_{mni} = \text{u}_1(i,m) \cdot \text{u}_1(i,n) - \Delta y_i \cdot \text{u}_2(i,m,n)$ $\text{dd2}^t = \sum_m \sum_n \sum_i v_{mi} D_{mni} v_{ni} = \sum_i \sum_m \sum_n v_{mi} v_{ni} D_{mni}$	$\text{dd2}^t = \mathbf{v}^{\mathbf{T}} \mathbf{v}$

Model Dependent

i – pixel
j – energy
l – material
t – iteration

Multimaterial   Linear

Input
y_i

Initialize
$\hat{x}^o$

Calculate
y_i' $y_i' = y_i - \sum_j B_{ij}' B_{ij} z_{ij}$ $y_i' = y_i$

Calculate
w^o $\mathbf{w}^o = \mathbf{A}\,\hat{\mathbf{x}}^o$

Calculate
$\tilde{y}_i^o$ $\tilde{y}_i^o = \sum_j B_{ij}' B_{ij} S_j \exp\left\{-\sum_l m_{lj} w_l^{oi}\right\}$ $\tilde{y}_i^o = w_i^o$

Calculate
Δy_i^o $\Delta y_i^o = y_i - \tilde{y}_i^o \left(= y_i - \hat{y}_i^o\right)$

Calculate
r^o $\left[r_m^o\right]_i = \Delta y_i^o \sum_j B_{ij}' B_{ij} S_j m_{mj} \exp\left\{-\sum_l m_{lj} w_l^{oi}\right\}$ $r_i^o = \Delta y_i^o$

Calculate
fn^o $fn^o = \frac{1}{2}\sum_i \left(\Delta y_i^o\right)^2$

$t = 0$

main loop

Calculate
g^t $\mathbf{g}^t = -\mathbf{A}^{\mathbf{T}}\mathbf{r}^t$

Yes $t = 0$?   No

Calculate
$\mathbf{d}^0 \approx -\mathbf{g}^0$

Check stopping conditions

Determine
β^t

Calculate
$\mathbf{d}^t \approx -\mathbf{g}^t + b^t \mathbf{d}^{t-1}$

Calculate
dd^t $dd^t = \mathbf{g}^t \cdot \mathbf{d}^t$

Figure 4a: Data flow for linear and nonlinear algorithms.

<u>Multimaterial</u>   <u>Linear</u>

```
┌──────────────┐
│  Calculate   │        $\mathbf{v}^t = -\mathbf{A}\mathbf{d}^t$
│    v t       │
└──────────────┘
       │
┌──────────────┐        $dd2^t = \sum_m \sum_n \mathbf{v}_m^{\mathbf{T}} \mathbf{D}_{mn} \mathbf{v}_n$          $dd2^t = \mathbf{v}^{\mathbf{T}} \mathbf{v}$
│  Calculate   │
│    dd 2 t    │
└──────────────┘
       │
┌──────────────┐     where,    $u_1(i,m) = \sum_j B'_{ij} B_{ij} S_j \boldsymbol{m}_{mj} \exp\left\{-\sum_l \boldsymbol{m}_{ij} w_l^i\right\}$
│  Calculate   │
│ initial v₂   │               $u_2(i,m,n) = \sum_j B'_{ij} B_{ij} S_j \boldsymbol{m}_{mj} \boldsymbol{m}_{nj} \exp\left\{-\sum_l \boldsymbol{m}_{ij} w_l^i\right\}$
└──────────────┘
       │                       $\mathbf{D}_{mni} = u_1(i,m) \cdot u_1(i,n) - \Delta y_i \cdot u_2(i,m,n)$
┌──────────────┐
│   v₁ = 0     │               $dd2^t = \sum_m \sum_n \sum_i v_{mi} D_{mni} v_{ni} = \sum_i \sum_m \sum_n v_{mi} v_{ni} D_{mni}$
└──────────────┘
       │
```

$\Delta v = v_2 - v_1$ (line search loop)

$$x(v_2) = x(v_1) + (v_2 - v_1)*d(v_1)$$

Check bounds on $x(v_2)$, Update $d(v_2)$

Matcol ?

$w(v_2) = A\,x(v_2)$
$v(v_2) = Ad(v_2)$

$w(v_2) = w(v_1) + \Delta v * v(v_1)$
matcol w and v

Calculate $\tilde{y}(v_2),\ r(v_2),\ fn(v_2),\ \Delta y(v_2),\ dd(v_2)$

$dd^t = \mathbf{r}^t \cdot \mathbf{v}^t$ $dd^t = \Delta \mathbf{y}^t \cdot \mathbf{v}^t$

Check   Done line search loop

$v_1 = v_2$

Select new v_2

$r^t = r(v_2)$ $dd^t = dd(v_2)$
$d^t = d(v_2)$ $fn^t = fn(v_2)$
$x^t = x(v_2)$ $\Delta y^t = \Delta y(v_2)$

$t = t + 1$

Figure 4b: Data flow for linear and nonlinear algorithms.
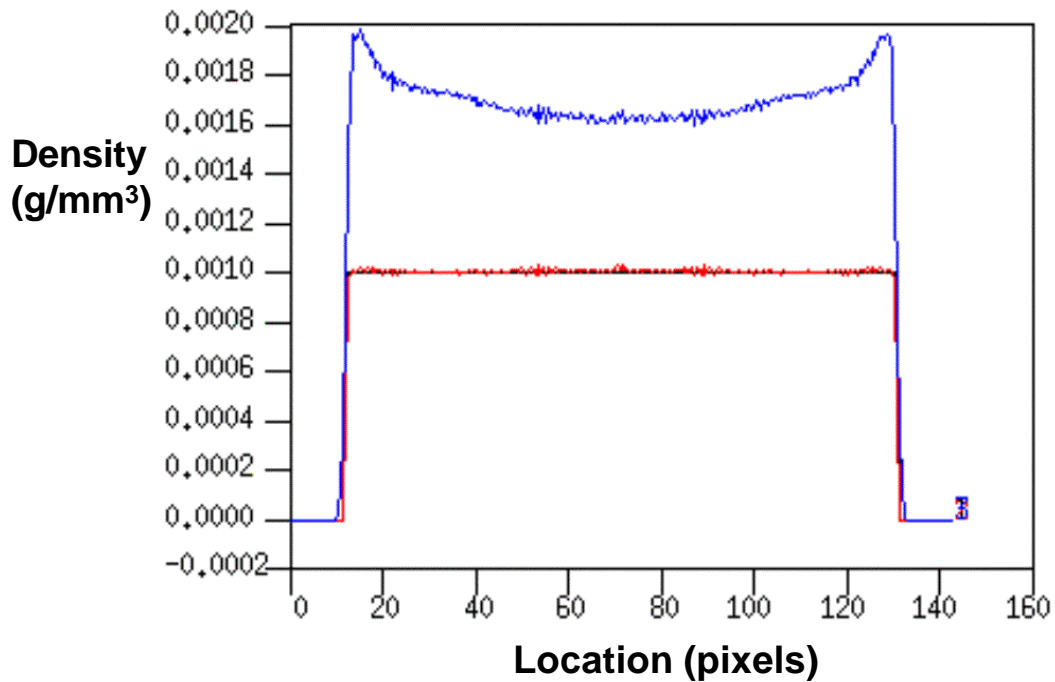
Figure 5: Comparison of reconstructed density profiles (blue and red) with actual cylinder density (black) for the central slice. The full nonlinear code (MCONE-CCG) produced the red curve, while a linear code (LCONE-CCG) produced the blue curve. For this figure and the next two, 180 views equally spaced between 0 and 360° were used. There were 300 horizontal rays and one vertical ray per view. The source to object distance was 5.792 m, while the source to detector distance was 6.090 m. The pixel size was 0.5 mm and the reconstruction voxel size was $(0.475 \text{ mm})^2$.
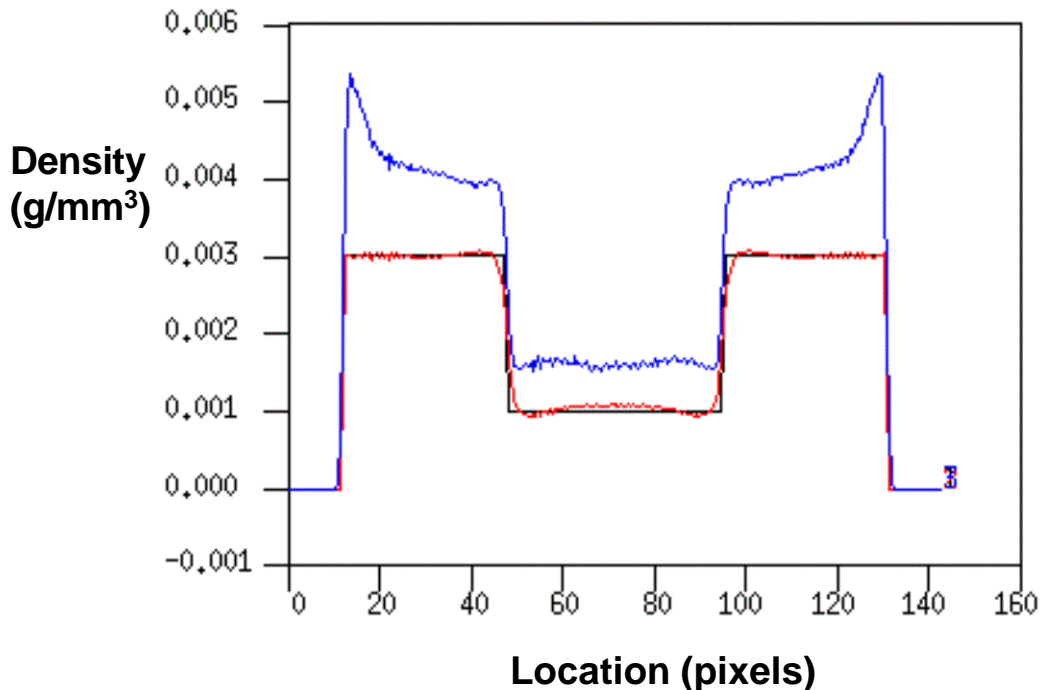
Figure 6: Comparison of reconstructed density profiles (blue and red) with actual cylinder density (black) for the central slice. The full nonlinear code (MCONE-CCG) produced the red curve, while a linear code (LCONE-CCG) produced the blue curve.
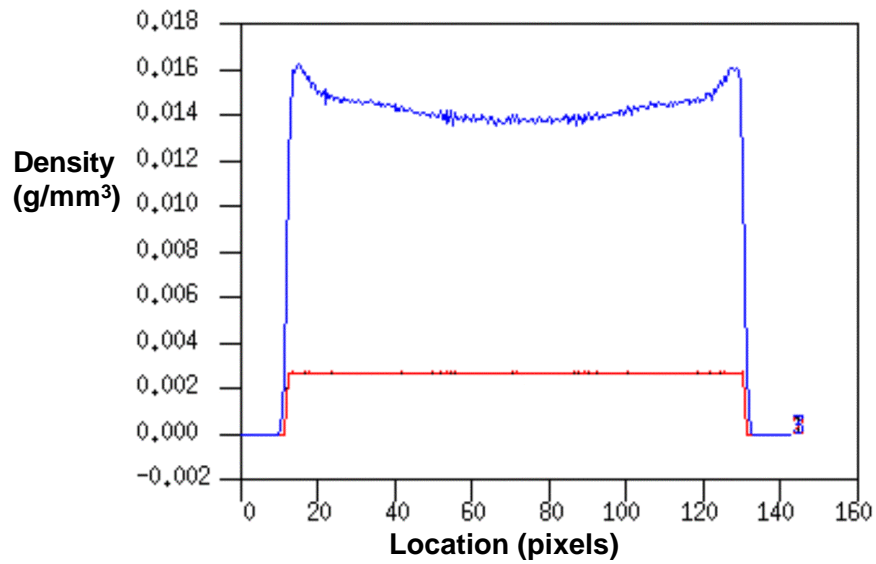
Figure 7: Comparison of reconstructed density profiles (blue and red) with actual cylinder density (black) for the central slice. The full nonlinear code (MCONE-CCG) produced the red curve, while a linear code (LCONE-CCG) produced the blue curve.
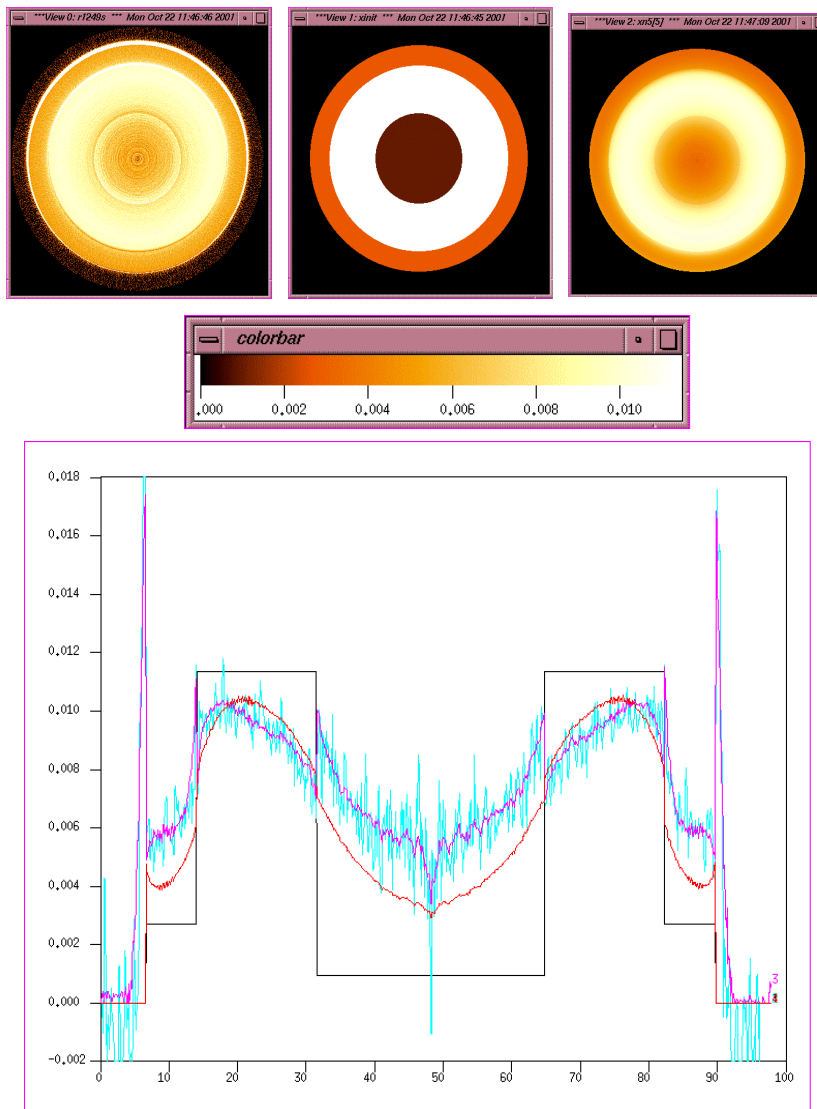
Figure 8: Comparison of reconstructions using real data. Top row are images of the central slice plane of the object. Left image is convolution back projection result, right image is nonlinear (MCONE-CCG) result, while center is the actual object. Below are density profiles. Black is original object, turquoise is convolution back projection reconstruction, magenta is linear (LCONE-CCG) reconstruction, and red is nonlinear (MCONE-CCG) reconstruction. For this figure, 600 views equally spaced between 0 and 360° were used. There were 840 horizontal rays and one vertical ray per view. The source to object distance was 5.492 m, while the source to detector distance was 6 m. The pixel size was 0.127 mm and the reconstruction voxel size was $(0.116247 \text{ mm})^2$.

Figure 9: The Stonehenge collimators with the Linetron 3000 X-Ray source in the foreground.

Appendix 1

Blurring Artifacts in Megavoltage Radiography With a Flat-Panel Imaging System: Comparison of Monte Carlo Simulations With Measurements, Schach von Wittenau et al., UCRL-JC-144247

Blurring artifacts in megavoltage radiography with a flat-panel imaging system: Comparison of Monte Carlo simulations with measurements

A. E. Schach von Wittenau, C. M. Logan, M. B. Aufderheide, III, and D. M. Slone

Lawrence Livermore National Laboratory, Livermore, CA 94550

(July 16, 2001)

Originally designed for use at medical-imaging x ray energies, imaging systems comprising scintillating screens and amorphous Si detectors are also used at the megavoltage photon energies typical of portal imaging and industrial radiography. While image blur at medical-imaging x ray energies is strongly influenced both by K-shell fluorescence and by transport of optical photons within the scintillator layer, at higher photon energies the image blur is dominated by radiation scattered from the detector housing and internal support structures. We use Monte Carlo methods to study the blurring in a notional detector: a series of semi-infinite layers with material compositions, thicknesses, and densities similar to those of a commercially available flat-panel amorphous Si detector system comprising a protective housing, a gadolinium oxysulfide scintillator screen, and associated electronics. We find that the image blurring, as described by a point-spread function (PSF), has three length scales. The first component, with a sub-millimeter length scale, arises from electron scatter within the scintillator and detection electronics. The second component, with a millimeter-to-centimeter length scale, arises from electrons produced in the front cover of the detector. The third component, with a length scale of tens of centimeters, arises from photon scatter by the back cover of the detector. The relative contributions of each of these components to the overall PSF vary with incident photon energy. We present an algorithm which includes the energy-dependent sensitivity and energy-dependent PSF within a ray-tracing formalism. We find quantitative agreement ($\sim 2\%$) between predicted radiographs with radiographs of copper step wedges, taken with a 9-MV bremsstrahlung source and a commercially available flat-panel system. The measured radiographs show the blurring artifacts expected from both the millimeter-scale electron transport and from the tens-of-centimeters length scale arising from the scattered photon transport. Calculations indicate that neglect of the energy-dependent blurring would lead to discrepancies in the apparent transmission of these wedges of the order of 9%.

I. INTRODUCTION

Amorphous Si detectors, paired with scintillating screens, are widely used for imaging at medical-imaging photon energies [1]. Because of their large active areas and ease of use, such systems are also being considered for radiography at the MeV photon energies (e.g., Refs [2–5]) found in portal imaging and in industrial radiography. One complication in interpreting the resulting radiographs at these higher energies, especially quantitatively, is that the images will frequently be degraded by blurring. While one source of blur in these systems is the transport of optical photons from the scintillating layer to the detector [2,6–9], it is well known that transport of secondary, high-energy, photons and electrons also needs to be considered when describing the response of these systems to x rays (e.g., Refs. [8,10–14]).

In practice, a screen/detector system consists of more than simply the screen and detector themselves. Practical systems also have protective housing, as well as internal support structures for the screen and detecting electronics. At megavoltage photon energies, scatter from these structures may significantly affect the imaging properties of the overall system.

In this paper we present Monte Carlo studies of a notional flat-panel detector, where the notional detector is a cylindrically-symmetric series of layers of materials with thicknesses, compositions, and densities representative of a commercially-available flat panel imaging system. Using a simulated 9-MV bremsstrahlung spectrum, we selectively disable particle transport mechanisms within the notional detector to understand how the various detector components contribute to the overall system blur. We next look at the photon-energy dependent sensitivity, blur, and detective quantum efficiency (DQE) of this detector, over the photon energy range of 20 keV to 10 MeV. We discuss the incorporation of the Monte Carlo results into a pre-existing ray tracing radiography simulation code. We calculate the image that would be obtained by radiographing a pair of Cu step wedges, assuming a 9 MV bremsstrahlung source and the notional detector. We compare this image with that obtained using a commercially-available 9 MV bremsstrahlung source and a flat-panel display. We close with a discussion of sources of scatter and background radiation that are not included in the raytracing approach.

II. METHODS AND MATERIALS

A. Experiments

1. Radiographic facility

Figure 1 shows a schematic of the experimental arrangement. The radiographic facility used for the measurements is a concrete-lined room approximately $12 \times 9 \times 12 \, \mathrm{m}^3$ (L × W × H), containing the x ray source, a series of fixed Pb collimators, and a stand to hold the detector. The source-to-detector distance is 6 m. Objects are placed at 5 m from the source. The fixed collimators are 1.5 m, 3 m, and 4.5 m from the source. The radiographic axis is 1.2 m above the floor. The Pb collimators are each 10 cm thick, with tapered, rectangular holes. The holes are focussed at the source position, and project at the detector position to a 27 cm × 40 cm area. This area is slightly smaller than the active area of the detector. The bremsstrahlung source for these experiments is a Linatron 3000 linac (Varian Inc., Palo Alto, CA), operating at 9-MeV nominal beam energy. Internal studies using a W-alloy rollbar have shown that the photon source spot is well-approximated by a Gaussian function 1.5 mm wide (full width at half-maximum height). The detector is the high-energy version of Flashscan 4030 (Varian Inc., Palo Alto, CA) array (an amorphous-Si area detector, with electronic readout) fitted with a Lanex-Fine screen (Kodak, Inc., Rochester NY). The Flashscan 4030 has a pixel pitch of $127\mu\mathrm{m}$, with the pixels arranged in a 3200×2304 array ($40.6 \times 29.3\mathrm{cm}^2$). The pixel fill factor is 57%.

2. Cu step wedges

Two Cu step wedges were radiographed. Both wedges have identical step profiles (Figure 2). The transmission of the step wedges ranges from approximately 40% to approximately 80% for a 9 MV bremsstrahlung spectrum. The wedges differ only in their widths: one wedge is 1.27 cm wide and the other is 5.08 cm wide. The wedges were designed to be approximately symmetric so that their scattered-radiation distribution would be approximately symmetric left-to-right and top-to-bottom. This near-symmetry is intended facilitate scatter-background subtraction from the resulting radiographs, should such a step be needed.

B. Simulation

Two software packages are used in this paper. The first is MCNP4C [15], a full-physics Monte Carlo code with extensive tallying capabilities. MCNP has user-settable flags to enable or disable physics processes in different portions of a user-specified geometry. Such flags are useful for evaluating which portions of the structure contribute, for example, to energy deposition in a given region. The MCNP4C [15] package is used for the Monte Carlo simulations of the bremsstrahlung spectrum from the 9 MV linac, for the simulations of the energy-dependent detector sensitivity, blur, and DQE, and for the full-physics simulations of the amount of room scatter. MCNP's software switches were used to (1) change the electron tracking algorithms from MCNP's default

'bin-centered' treatment to the 'nearest group boundary' method; and (2) to generate internal electron cross section tables only for the electron energy range appropriate to the particular simulation, rather than using MCNP's default value of 100 MeV. The motivations for using these switches are discussed in Refs. [16,17].

A locally-written ray-tracing code HADES [18–20] is used to simulate radiographs of the step wedges. The HADES code simulates radiographs by raytracing through objects, which may be described either using simple geometric surfaces or by any of a number of standard voxel-based meshes. A ray is traced from the source position to the center of each pixel (m, n) of the detector. For each such ray, all intersections with specified objects are calculated, and the total attenuation pathlength $P_{m,n}$ is calculated:

$$P_{m,n} = \sum_i \rho_i \mu_i \lambda_{i,m,n} \qquad (1)$$

where the summation over i is over all objects or mesh voxels intersected by the $(m, n)^{\text{th}}$ ray. Each object or voxel i has mass scattering coefficient μ_i and density ρ_i. The mass scattering coefficients are derived from the photon scattering cross sections given in Ref. [21]. $\lambda_{i,m,n}$ is the pathlength of the $(m, n)^{\text{th}}$ ray through object or cell i.

For the case of radiography with a polyenergetic photon sources, such as a bremsstrahlung source, the energy dependences of the μ_i become relevant. In this case, HADES calculates, for each energy E_j in the source spectrum, an energy-dependent total pathlength $P_{j,m,n}$, where

$$P_{j,m,n} = \sum_i \rho_i \mu_{i,j} \lambda_{i,m,n} \qquad (2)$$

Once the $P_{j,m,n}$ have been calculated for all energies j and for all pixels (m, n), the energy-dependent pixel 'signals' $T_{m,n}$ may be calculated:

$$T_{m,n} = \sum_j N_{j,m,n} e^{-P_{j,m,n}} \qquad (3)$$

where $N_{j,m,n}$ is the number of photons with energy E_j that would be incident on the $(m, n)^{\text{th}}$ pixel if no objects were present. The final image I is then the collection of the individual pixel signals:

$$I = (T_{m,n}) \qquad (4)$$

The image I is usually normalized by a 'no-object' image $I_\circ$, where

$$I_\circ = \left(\sum_j N_{j,m,n} \right) \qquad (5)$$

thus yielding a relative transmission image $I/I_\circ$.

Given a library of source spectra, with each spectrum being characteristic of a specific x-ray source, the user can simulate radiographs that would be obtained with those photon sources.

C. Generation of the 9 MV bremsstrahlung spectrum

Monte Carlo methods are widely used for generating output photon spectra for MV-energy bremsstrahlung sources (e.g., Refs. [16,22–30]). Such spectra have then been used as input to photon teletherapy dose calculations. Good agreement has been found between these calculations and measurements of dose in water phantoms when the original bremsstrahlung simulations are performed using the nominal electron beam energy. For precise clinical work, however, the electron beam energy is usually adjusted slightly to improve that agreement.

To simulate the 9 MV bremsstrahlung spectrum of our 9 MV linac, MCNP4C was used to obtain the photon output of a monoenergetic, zero-width beam of 9-MeV electrons incident normal to a 0.175 cm thick W target, which was in turn backed by a 0.225 cm thick copper layer. The target was surrounded by a W cylinder to simulate the shielding inside the accelerator housing. There is a conical primary collimator downstream of the target. Because we were also interested in estimating the levels of scattered radiation from the collimators, etc, these structures were included in the simulations. Approximately 1.5×10^7 electrons were run. As a variance reduction measure, bremsstrahlung photons were sampled at each electron step. Kinetic energy tracking cutoffs were 10 keV for photons and electrons. Photons were tallied using a point detector (next-event estimator) located six meters downstream. The tally was subdivided to show the origins of the radiation reaching the point detector. Results are given in Table I.

Three types of photon scoring are shown: a number-weighted scoring, an energy-weighted scoring, and a flat-panel detector-weighted scoring. (The flat-panel detector-weighted scoring is discussed in Section VII below). All three scoring methods indicate that the bremsstrahlung target and the primary collimator together contribute more than 98.7% of the radiation reaching the detector location. Radiation scattered from the Pb collimators (and their supporting framework) represents less than 0.2% of the total. Radiation scattered from the air and from the room itself represents a percent or less of the total.

Given our experimental geometry, which demagnifies the source size by a factor of five, we treat the photons from the bremsstrahlung target and from the primary collimator as coming from a single point source; and we use the energy spectrum of these photons for our subsequent raytracing simulations. Figure 3 shows the photon energy spectrum used.

III. MONTE CARLO STUDIES OF THE NOTIONAL DETECTOR

Our notional detector is a cylindrically-symmetric series of layers of materials with thicknesses, compositions, and densities representative of those found in commercially-available flat panel imaging systems. Table II lists the nominal parameters used for this paper. These nominal parameters are based on information obtained from manufacturers of flat-panel systems and from the manufacturers of components of such systems.

The front protective cover of our notional detector is a carbon-fiber sheet. There is an air gap between the front cover and the scintillating screen. The scintillating screen is made of gadolinium oxysulfide (33 mg/cm^2 loading) and binder on a plastic substrate. The screen has a thin protective coating on both sides. Next comes the glass substrate, onto which are deposited the Si-based electronics (we neglect the very thin electronics layer in our simulations). There is a polypropylene pad, followed by an aluminum support plate. These in turn are followed by an air gap for passage of wires. The last item is the aluminum back cover of the detector housing.

We assume that the output response of the notional detector is proportional to the amount of energy deposited in the scintillator layer. This energy deposition occurs during the cascade of photons and electrons derived from the interaction of each incident high-energy photon with the various components (protective housing, scintillating screen, etc.) of the detector. In real detectors, there are additional effects arising from the non-proportionality of the scintillation response as a function of electron energy [31, 32], from the transport of optical photons from the scintillator layer to the electronics, from the spatial nonuniformity in the electronics layer (necessary for having pixels), and from the non-unity pixel fill factor [33].

Before proceeding with the Monte Carlo studies, it is useful to consider the distribution of areal mass within the notional detector. The total areal density is ~ 2.6 g/cm^2. The front cover accounts $\sim 9\%$ of the total. There is a low-density region between front cover and the scintillator layer; this region is approximately 7 mm long. The scintillator layer accounts for $\sim 1.4\%$ of the total areal mass. The scintillator layer is followed by the glass substrate for the electronics, a polypropylene pad, and a layer of aluminum; these layers account for $\sim 62\%$ of the total areal mass. There is next another low-density region approximately 2 cm in length. Finally, there is the back cover, which accounts for $\sim 26\%$ of the total areal mass.

In the context of megavoltage radiography, this distribution of areal mass has significant implications for image blurring. At megavoltage energies, the dominant photon scattering mechanism is Compton scattering. To first order (neglecting the effects of atomic number on the cross sections), the scattering is proportional to the electron density of the materials being traversed by the

photon. Based on the parameters in Table II, then, only about 1.4% of the initial photon scattering will occur in the scintillator layer. Approximately 9% of the initial photon scattering occurs in the front cover of the detector system. In what is essentially a forward-scattering geometry, the scattered photon and Compton electron have to travel approximately 7 mm before interacting with, and depositing energy in, the scintillating layer. The radial extent of these contributions to the energy deposition in the scintillating layer would be several millimeters. (We note that Refs. [34, 35] discuss the effects on image quality of photon scattering by front covers of radiography cassettes.) Approximately 88% of the areal mass, and therefore, of the photon scattering, occurs downstream of the scintillating screen and detection electronics. Many of these scattering events occur several millimeters, if not several centimeters, from the scintillating screen. Contributions from the downstream support structures would be large-angle backscattering events, and would create a long-range length scale energy deposition background at the scintillator layer.

To study the radial distribution of these various energy depositions, MCNP4C was used to tally the energy deposition, as a function of distance from the symmetry axis, in the scintillating layer of the notional detector. (Generating such radial energy deposition tallies is a widely-used approach for modeling detector behavior. See, for example, Refs. [11, 36–38].) A zero-width photon beam was normally incident on the front cover. The energy distribution of the photon beam was that shown in Fig. 3. Kinetic energy tracking cutoffs were 1 keV for both photons and electrons, and 5×10^7 source photons were generated. Fig. 4(a) shows the resulting energy deposition as a function of radial distance. Fig. 4(b) shows the running integral of the energy deposition.

Figs. 4(a) and 4(b) indicate that the energy deposition in the scintillator layer has several length scales. The first length scale, with a radial extent of 0.5 mm, accounts for approximately 37% of the energy deposited in the scintillator layer as a whole. The second length scale goes from approximately 0.5 mm to 1 cm, and accounts for approximately 46% of the energy deposited in the scintillator. The third length scale goes from approximately 1 cm to 25 cm. This last distribution accounts for the remaining 17% of the energy deposited in the scintillator.

The software switches in MCNP4C can be used to investigate the origins of the length scales. Setting all the materials in the system, except for the scintillating screen and the glass substrate, to be vacuum gives the energy deposition that would occur if these layers could be freestanding in a real system. Fig. 5a shows the results. Thus, the radial extent of the energy deposited in the scintillator, outside a radius of 5.5 mm, is due primarily to the detector covers and to the aluminum plate supporting the glass layer.

Fig. 5(b) shows the energy deposition pattern which results if electron transport is disabled everywhere in the notional detector. With electron transport disabled, pho-

tons can be scattered, but electrons deposit all their energy at the location of the collision. Energy deposition in the first tally cylinder is increased (the daughter electrons now deposit all their energy in this cell). Only the longest length scale process is preserved, suggesting that scattered photons cause the long range tail in the energy deposition.

Given that the short-range energy depositions are not due to scattered photons, these depositions are due to scattered electrons. Fig. 5(c) shows the energy deposition pattern obtained if electron production and transport are disabled in the front cover and in the first air gap. The length scale from 0.5 mm to 1 cm disappears, suggesting that this length scale is caused by daughter electrons produced in those regions. Fig. 5(d) shows the energy deposition pattern obtained if photon and electron transport are disabled in the back cover of the detector. There is some decrease in the energy deposition at length scales less than 1 cm, but the long-range tail from the scattered photons is reduced.

We conclude that the energy deposition at a radial distance less than ∼ 0.5 mm is due to electron transport within the scintillator. Transport of electrons from the front cover to energy deposition at radial distances between ∼ 0.5 mm and ∼ 1 cm. The long range energy deposition is due to photon scatter by the back cover.

IV. VARIATION OF DETECTOR RESPONSE WITH PHOTON ENERGY

The above discussion of blur was for the specific case of a 9-MV bremsstrahlung photon beam. To study the detector behavior as a function of photon energy, MCNP4C was used to model a series of monoenergetic photon pencil beams incident on the above-described stack of materials. The outer diameter of the notional detector was set to 50 cm (the length of the diagonal of the illuminated area of our detector). The energy of the incident photons was varied from 20 keV to 10 MeV. Kinetic energy tracking cutoffs were 1 keV for both photons and electrons. Various tallies of the energy deposition in the scintillator layer were made. The tallies are described below.

A. Total energy deposition in scintillator layer

Figure 6 shows the amount of energy deposited, per incident photon, in the scintillator layer as a whole, as a function of photon energy. Starting at 20 keV, the energy deposit generally decreases as the photon energy increases, up to around 500 keV. There are sharp jumps in the energy deposit as the photon energy sweeps above the K edges of some of the constituent elements in the detector. The noticeable jumps occur at ∼ 37.4 and ∼ 50.2 keV, which are the K-edge thresholds for Ba (in

the glass substrate) and for Gd (in the scintillator), respectively. The energy deposition curve is relatively flat for photon energies above 500 keV.

B. Energy-dependent detective quantum efficiency (DQE)

If each incident photon always deposited energy in the scintillator, and if the energy deposit was the same for each photon of a given energy, then the statistics of the image would be given by the variability of the incident photon fluence. Thus, for an average number of particles N, the ideal detector would have [39] a signal-to-noise ratio (SNR)

$$SNR_{ideal} = \sqrt{N} \qquad (6)$$

In the notional detector, however, the energy deposition in the scintillator layer comes from the cascade of photons and electrons produced by the incident photon. The energy deposition per incident photon will therefore vary from photon to photon. The effect of the variability in energy deposition is to increase the noise in an image, above what would be expected if the each incident photon always deposited the same amount of energy in the scintillator. This increase in noise defines the detective quantum efficiency (DQE), where [39]

$$DQE = \left[\frac{SNR_{actual}}{SNR_{ideal}} \right]^2 \qquad (7)$$

It can be shown [39, 40] that the DQE can be calculated from the moments of the pulse-height distribution:

$$DQE = \frac{m_1^2}{m_0 m_2} \qquad (8)$$

where m_0, m_1, and m_2 are the zeroth, first, and second moments of the pulse height distribution in the scintillator layer. In the same Monte Carlo runs described above, a tally was kept for the pulse-height distribution of the energy deposited in the scintillator layer. The moments of these distributions were calculated as a post-processing step. Figure 7 shows how the resulting DQE varies with photon energy for the notional detector.

C. Radial extent of energy deposition

For the purposes of studying the radial variation of the energy deposition, the scintillator layer was subdivided by cylinders of logarithmically-varying radius. The energy deposited within each subregion of the scintillating layer was tallied. Fig. 8a shows the radius required to include 99% of the energy deposited within the scintillating layer. Starting at the lowest energy considered (20 keV), the curve shows a gradual increase in the radial extent of the energy deposition. At 50.2 keV, the photoelectric absorption cross section for Gd is reached.

At this point, there is a jump in the probability for photoabsorption in the scintillator layer, with the photoelectron depositing its energy in the scintillator layer. Correspondingly, a smaller fraction of the energy deposited is included in the tail of the distribution. As the photon energy increases, there is a continuous increase in the radial extent of the energy deposition until the photon energy is approximately 400 keV. At this point, electrons from the front shield start having enough energy to reach the scintillator layer. These electrons deposit energy within a centimeter of the original photon beam. Although there is still a long-range tail due to scattered photons, this tail makes up proportionally less of the total energy deposited, and the (normalized) PSF becomes narrower. This apparent narrowing of the PSF continues as the photon energy increases to about 2 MeV, at which point progressively more energy is deposited into the tail of the PSF.

Fig. 8a shows that a maximum tally radius of 28 cm is adequate for accounting for 99% of the deposited energy for the photon energies considered (20 keV to 10 MeV). By extension, such a tally radius would be adequate for any linear combination of photon energies within that energy range. Such linear combinations of photon energies would describe, for example, the output energy distribution of a bremsstrahlung source, or the energy distribution of photons exiting the object being radiographed. Using smaller tally radii, as shown in Fig. 8b, would lead to significant, energy-dependent, errors in the calculated energy response of the detector.

V. TREATING PHOTON-ENERGY-DEPENDENT DETECTOR EFFECTS WITHIN A RAYTRACING MODEL

It is useful to include detector effects within a radiography simulation code, so that users can evaluate the trade-offs involved when choosing or designing a particular detector system for a given radiographic experiment. It is also helpful if these detector effects can be treated reasonably accurately within the context of a fast raytracing code. If the effects that are included are those found for the case of our notional detector, it is worth noting that we are excluding effects arising from such things as the transport of optical photons in the scintillator layer, as well as the effects of pixelation fill-factor. We also are assuming that all photons are incident normal to the detector. For our experimental geometry, the photons from the bremsstrahlung source have incident angles within 2° of the surface normal. We assume that the behavior of the detector is linear, isotropic, and isoplanatic. With these assumptions, incorporation of energy-dependent effects becomes straightforward.

The complete set of (m, n) values $T_{m,n}$ in Eq. 4 forms a radiographic image I. The radiographic image I can expressed as a sum of j sub-images, where each sub-image is specific to a particular photon energy E_j:

$$I = (T_{m,n}) = \sum_j T_{m,n,j} \tag{9}$$

$$= \sum_j (T_{m,n,j'} \parallel j' = j) \tag{10}$$

where, as before,

$$T_{m,n,j} = N_j e^{-P_{j,m,n}} \tag{11}$$

The inclusion of energy-dependent detector effects is accomplished by operating on the individual, monoenergetic sub-images before the recombination step which creates the final image.

A. Energy-dependent detector sensitivity

If the detector has an energy dependent response D_j for a given energy E_j, Eqs. 3 and 5 become, respectively,

$$I = (T_{m,n}) = \left(\sum_j N_j D_j e^{-P_{j,m,n}} \right) \tag{12}$$

$$I_\circ = \left(\sum_j N_j D_j \right) \tag{13}$$

With our assumption that the detector response is proportional to the energy deposited in the scintillator layer (i.e., by neglecting any nonlinearity in the scintillator response, and by neglecting variations in the transport of optical photons), the D_j of Eq. 12 are the energy depositions shown in Fig. 6.

Fig. 9 shows the results of raytracing simulations of the transmissivity of the Cu step wedge for three different assumed energy sensitivity relations for the detector. The photon spectrum is that shown in Fig. 3. The first simulation assumed a flat energy response (i.e., where the D_j of Eq. 12 are all equal to unity). Such an energy response is an approximation to that of a thin detector. The second curve shown in Fig. 9 assumed an energy response $D_j \propto E_j$ (i.e., where all the photon energy is deposited in the detector). Such an energy response is an approximation to that of a thick detector such as a block of scintillator material. The third curve in Fig. 9 is for the energy response curve of Fig. 6.

These plots show that a thick detector, with a response proportional to energy, would show the highest transmission for the Cu step wedge. If the detector response is proportional only to the number fluence, the apparent transmission drops when the incident photon spectrum has more low energy photons than high energy photons. If the detector is more sensitive to low-energy photons than to high-energy photons, the apparent transmission decreases still more. Given that most of the photons in the spectrum shown in Fig. 3 are in the relatively flat portion of the curve shown in Fig. 6, the notional detector's transmission is close to that of a fluence counter.

B. Energy-dependent DQE

In cases where the image quality is dominated by the statistics of the incident photons, the DQE values of Fig. 7 may be applied to each of the energy bins used to represent the photon spectrum. Photon-limited experiments include flash radiography, where the the user has to consider the specific number of photons per pulse produced by an x ray head [41]. Given the known photon output of the accelerator head and the geometry to be used for the measurement, as well as details of the object to be radiographed, the mean number of photons N_j with energy E_j reaching a particular pixel can be calculated using Eq. 1. If the detector were ideal, the actual number of photons per pixel would be sampled from a Poisson distribution with mean N_j. For the notional detector, with the DQE values of Fig. 7, a Poisson distribution with a mean of $(DQE \times N_j)$ is sampled instead. The thus-obtained Poisson deviate is then divided by the DQE in order to preserve the average photon fluence.

C. Energy-dependent image blur

To account for an energy-dependent blurring on the part of the detector, we blur the sub-image for each energy individually before summing the results according to Eq. 10 to form the total image. With the assumptions of (a) normally-incident photons, and (b) an isoplanatic and isotropic detector response, the blurring becomes a convolution of the initial sub-images with a point-spread function (PSF), where the PSF used is appropriate to the photon energy of the specific sub-image. Eq. 10 thus becomes:

$$I = (T_{m,n}) = \left(\sum_j T_{m,n,j} \right) \qquad (14)$$

$$= \left(\sum_j (T_{m,n,j'} \parallel j' = j) \circ PSF_j \right) \qquad (15)$$

Although the PSF is not tallied during the Monte Carlo runs, the radial distributions of the energy depositions are tallied. The pixel sizes are specified by the user performing the radiographic simulation. Since the pixel sizes may vary from one simulation to another, the remapping of the radial energy tallies onto the pixel array occurs at run-time. For each pixel in the Cartesian mesh, the fraction of each tally volume is contained by the intersection of the particular pixel and that tally cylinder is calculated based on the corresponding overlap integral. If all of the energy-specific Monte Carlo simulations are performed using the same set of tally radii, then the remapping integrals need be calculated only once. The values can be reused for each subsequent energy group. Once the PSF has been generated for the particular energy, the convolution is done using standard FFT methods [42].

Figure 10 shows the effect of blur on the apparent transmission of the Cu step wedges. Recall that the blur has both a short range component (millimeter in length scale) and a long-range component (several centimeters to several tens of centimeters in length scale). The millimeter-length scale blur has the effect of rounding the edges of the steps. The centimeter-scale blur has the effect of increasing the amount of energy deposited in the scintillator, in the area normally shaded by the step wedges. The apparent transmission of the step wedges is changed. The degree of change is affected by the width of the step wedges (given that the wedges have identical step profiles, in the absence of blurring effects, they would both have the same apparent transmission). The thinner of the two wedges has its minimum estimated transmission increased by $\sim 9\%$; the thicker of the two wedges has its minimum estimated transmission increased by $\sim 4\%$.

VI. COMPARISON WITH MEASUREMENTS

At this point it is useful to compare the calculations shown in Figure 10 with actual measurements. The flat-panel detector was first calibrated by taking three images at different levels of irradiation for equal-length times: a dark field image (accelerator turned off), a mid-field image (the accelerator operated at $\sim 60\%$ power by modifying the pulse-repetition frequency), and a high-field image (accelerator operated at full power). After acquisition of a specific radiograph, the conversion of pixel signal to exposure level was performed on a pixel-by-pixel basis, using linear interpolation between the mid- and dark-field measurements, or the high- and mid-field measurements, depending on the experimental signal level of the particular pixel. Note that this procedure implicitly corrects for (a) local variations in scintillator response, (b) sensitivity of the electronics, and (c) spatial variation in the photon intensity. A radiograph was taken of both wedges (Fig. 11). The wedges are clearly visible, along with mounting brackets and screws near the bottom of the image. The image was normalized by rescaling the signal at the center point to match the calculated transmission at the same location on the calculated image. No other operations (e.g., background estimation or subtraction) were performed. The lineouts along the centerlines of each wedge from both the measured and calculated images were extracted. The lineouts are shown in Fig. 12.

VII. DISCUSSION

The rounding of the individual steps, predicted based on the blurring characteristics of the notional detector, is clearly visible in both of the experimental lineouts. This rounding was expected because of short-range blurring. The experimental lineouts also show different apparent

transmissivities, even though the two wedges have identical profiles (Fig. 2). Given that the narrower wedge is 1.27 cm wide, this difference in transmissivities is consistent with a significant portion of the x ray energy being scattered from further than 5 mm (Fig 4).

There is a systematic difference between the predicted and measured lineouts, however. The predicted lineouts show too high a transmissivity near the ends of the step wedges, and slightly too low a transmissivity at the centers of the lineouts. These differences could be due to errors in the shape of the photon spectrum (the spectrum was calculated assuming the nominal electron beam energy, and was not adjusted to improve the agreement), in the shape of the detector sensitivity curve (the parameters used for our notional detector are not necessarily those of the real detector), or in the blurring functions. Nonetheless, the differences between the calculated and measured lineouts for each wedge are smaller than the differences between the two experimental lineouts themselves.

While the agreement between the calculated and measured curves of Fig. 12 is generally good, it is worth noting that the calculations neglect the effects of scattered radiation.

One source of scatter background would be the wedges themselves. In other work, we have made radiographs of these wedges at a much closer object-to-detector distance. The scatter background in those images was significant. Analysis of these images indicated that moving the wedges further from the detector, to the 1 m object-to-detector distance used here, would reduce to scatter background from the wedges to below 1%.

A second background source is photon scatter from the various collimators, supporting structures, as well as from the room air and the room walls. We have performed Monte Carlo simulations, described in Section II C, of the radiography facility in order to quantify sources of scattered photons arriving at the center point of the detector. Results are listed in Table I. Three different detector sensitivities are assumed: a flat energy response, corresponding to a thin detector; a linear energy response, corresponding to a thick detector; and the energy response shown in Fig. 6. For all three cases, at least $\sim 99\%$ of the detector signal is due to radiation from the bremsstrahlung target, target backing, and primary collimator. Photon radiation scattered by the room, the collimating structures, and the air accounts for less than 1% of the detector signal.

A third source of scatter-background is from electrons. High-energy photon beams are accompanied by contaminant electrons, and in photon teletherapy these electrons contribute a non-negligible fraction of the surface dose in water phantoms [43–46]. The dose from contaminant electrons extends several millimeters into the water. Thus, for high-energy photon beams, electrons still contribute to dose after passing through a significant fraction of a gram of areal mass. From Table II, we see that there is 0.24 g/cm^2 of areal mass upstream of the scintillator layer. We thus expect some dose to the scintillator layer from contaminant electrons. Since we assume that the detector signal is proportional to the energy deposited in the scintillator, we thus expect that the detector should register a background from these electrons.

To estimate the size of this effect, we performed two MCNP4C simulations of a simplified source/collimator/detector geometry. These simulations included the Pb collimators and the room air, but omitted the room walls, the collimator support structures, and the accelerator housing and collimator. The detector was modeled as a series of slabs (40 cm × 27 cm) of the appropriate materials and thicknesses. The source particles were photons whose energies were sampled from the distribution shown in Fig. 3. The energy deposited in the scintillator layer was tallied. In the second calculation, electrons produced upstream of the detector were 'killed' just before they interacted with the detector assembly. The difference in energy deposition between the two runs was $\sim 8\%$.

Such a background level would increase the apparent transmission of the step wedges, more so at the thickest portions of the wedges. A 45% transmission would become a 49% transmission ($(0.45 + 0.08)/(1.0 + 0.08) \approx 0.49$), whereas an 80% transmission would become a 81.5% transmission. Such a correction is in the direction required in Fig. 12, but is too large. Only a 2% correction is needed, assuming that the rest of the problem has been properly treated.

Our studies of the notional detector neglected the transport of optical photons from the scintillator layer to the amorphous Si layer. Such transport would affect both the energy-dependent image blur of the detector, as well as the energy-dependent detector response. Including the transport of optical photons would increase the predicted amount of image blurring, as the images would have to be convolved with the appropriate point spread function. Computer and experimental studies [6, 7, 47] of the line spread functions and of the modulation transfer functions of scintillating screens indicate that the screen blur is significantly less than 1 millimeter in radial extent (assuming cylindrical symmetry, conversion between MTFs, LSFs, and PSFs is straightforward [48,49]). Such blur is approximately the same size as the pixel size used in our calculations ($254 \mu m$). Optical photon transport within the scintillator layer affects the energy-dependent detector response via the escape probability of those photons to the detector layer: optical photons produced further from the detector layer are less likely to be create a signal. Such a depth dependence would be most apparent at low photon energies (less than a few hundred kilovolts), where the Gd cross section is high enough [21] that the scintillator layer is no longer radiographically thin. For our assumed spectrum (Fig. 3), however, more than 99% of the photons are above such an energy. Thus, optical photon transport would be a percent-level effect for the problem at hand.

VIII. CONCLUSION

Monte Carlo simulations indicate that radiation scattered from the various non-detector portions of a flat-panel detector system should be a significant source of image degradation at MV photon energies. Using the simplifying assumptions that the photons are normally incident onto an isotropic, isoplanatic detector, the results of the Monte Carlo simulations of detector behavior can be incorporated into a raytracing code. Predictions of this code are in reasonable quantitative agreement with step-wedge measurements. Such agreement is useful from the points-of-view of simulating experiments, as well as for scoping studies in detector design. There remain systematic disagreements between our predictions and the measurements. These may be due to lack of inexact knowledge of the internal structure of our detector, as well as to inexact knowledge of the photon spectrum from our linac. Effects not included in the raytracing approach, such as source spot blur and optical photon transport within the scintillator layer, are expected to be small, given our experimental arrangement.

[1] M. J. Yaffe and J. A. Rowlands, "X-ray detectors for digital radiography," Phys. Med. Biol. **42**, 1–39 (1997).

[2] P. Munro and D. C. Bouius, "X-ray quantum limited portal imaging using amorphous silicon flat-panel arrays," Med. Phys. **25**, 689–702 (1998).

[3] L. E. Antonuk, J. Yorkston, W. Huang, H. Sandler, J. H. Siewerdsen, and Y. El-Mohri, "Megavoltage imaging with a large-area, flat-panel, amorphous silicon imager," Int. J. Radiat. Oncol. Biol. Phys. **36**, 661–672 (1996).

[4] L. E. Antonuk, J. Boudry, W. Huang, D. L. McShan, E. J. Morton, J. Yorkston, M. L. Longo, and R. A. Street, "Demonstration of megavoltage and diagnostic x-ray imaging with hydrogenated amorphous silicon arrays," Med. Phys. **19**, 1455–1466 (1992).

[5] L. E. Antonuk, J. Yorkston, J. Boudry, M. J. Longo, J. Jimenez, and R. A. Street, "Development of hydrogenated amorphous silicon sensors for high energy photon radiotherapy imaging," IEEE Trans. Nucl. Sci. **37**, 165–170 (1990).

[6] C. Kausch, B. Schreiber, F. Kreuder, R. Schmidt, and O. Dössel, "Monte Carlo simulations of the imaging performance of metal plate/phosphor screens used in radiotherapy," Med. Phys. **26**, 2113–2124 (1999).

[7] J. M. Sabol and J. M. Boone, "Monte Carlo simulation of photon transport within a hybrid grid-detector system for digital mammography," Proc. SPIE **3032**, 266–274 (1997).

[8] H. P. Chan and K. Doi, "Studies of x-ray energy absorption and quantum noise properties of x-ray screens by use of Monte Carlo simulation," Med. Phys. **11**, 37–46 (1984).

[9] C. E. Metz and K. Doi, "Transfer function analysis of radiographic imaging systems," Phys. Med. Biol. **24**, 1079–1106 (1979).

[10] J. M. Boone, M. H. Buonocore, and V. N. Cooper, III, "Monte Carlo validation in diagnostic radiological imaging," Med. Phys. **27**, 1294–1304 (2000).

[11] J. M. Boone, J. A. Seibert, J. M. Sabol, and M. Tecotzky, "A Monte Carlo study of x-ray fluorescence in x-ray detectors," Med. Phys. **26**, 905–916 (1999).

[12] J. Yorkston, L. E. Antonuk, Y. El-Mohri, K. W. Jee, W. Huang, M. Maolinbay, X. Rong, J. H. Siewerdsen, and D. P. Trauernicht, "Improved spatial resolution in flat-panel imaging systems," Proc. SPIE **3336**, 556–563 (1998).

[13] B. A. Arnold and B. E. Bjärngard, "The effect of phosphor K x-rays on the MTF of rare-earth screens," Med. Phys. **6**, 500–503 (1979).

[14] R. K. Swank, "Calculation of modulation transfer functions of x-ray fluorescent screens," Appl. Opt. **12**, 1865–1870 (1973).

[15] J. F. Briesmeister, "MCNP^{TM}— a general Monte Carlo n-particle transport code," Technical Report LA-13709-M, Los Alamos National Laboratory (2000).

[16] J. V. Siebers, P. J. Keall, B. Libby, and R. Mohan, "Comparison of EGS4 and MCNP4b Monte Carlo codes for generation of photon phase space distributions for a Varian 2100C," Phys. Med. Biol. **44**, 3009–3026 (1999).

[17] R. Jeraj, P. J. Keall, and P. M. Ostwald, "Comparisons between MCNP, EGS4 and experiment for clinical electron beams," Phys. Med. Biol. **44**, 705–717 (1999).

[18] M. B. Aufderheide, III, D. M. Slone, and A. E. Schach von Wittenau, "HADES, a radiographic simulation tool," in D. O. Thompson and D. E. Chimenti (editors), "Review of Progress in Quantitative Nondestructive Evaluation, Vol. 20A," 507–513 (2001), AIP Conf. Proc. #557.

[19] H. E. Martz, Jr., M. B. Aufderheide, III, J. M. Hall, A. E. Schach von Wittenau, D. M. Goodman, C. M. Logan, J. A. Jackson, and D. M. Slone, "HADES-CCG, a new tomographic reconstruction tool," in D. O. Thompson and D. E. Chimenti (editors), "Review of Progress in Quantitative Nondestructive Evaluation, Vol. 20A," 724–731 (2001), AIP Conf. Proc. #557.

[20] D. M. Slone, M. B. Aufderheide, III, and A. E. Schach von Wittenau, "Radiographic simulations and

analysis for ASCI," in B. H. *et al.* (editor), "Proc. Ninth SIAM Conf. Parallel Proc. Sci. Comp.", (Society of Industrial and Applied Mathematics, Philadelphia, 1999).

[21] D. E. Cullen, H. M. Chen, J. H. Hubbell, S. T. Perkins, E. F. Plechaty, J. A. Rathkopf, and J. H. Scofield, "Tables and graphs of photon-interaction cross sections from 10 eV to 100 GeV derived from the LLNL evaluated photon data library (EPDL)," Technical Report UCRL 50400 Vol. 6 Rev 4, Lawrence Livermore National Laboratory (1989).

[22] M. K. Fix, M. Stampanoni, P. Manser, E. J. Born, R. Mini, and P. Rüegsegger, "A multiple source model for 6 MV photon beam dose calculations using Monte Carlo," Phys. Med. Biol. **46**, 1407–1427 (2001).

[23] D. Sheikh-Bagheri, D. W. O. Rogers, C. K. Ross, and J. P. Seuntjens, "Comparison of measured and Monte Carlo calculated dose distributions from the NRC linac," Med. Phys. **27**, 2256–2266 (2000).

[24] W. van der Zee and J. Welleweerd, "Calculating photon beam characteristics with Monte Carlo techniques," Med. Phys. **26**, 1883–1892 (1999).

[25] C. M. Ma, E. Mok, A. Kapur, T. Pawlicki, D. Findley, S. Brain, and K. Forster, "Clinical implementation of a Monte Carlo treatment planning system," Med. Phys. **26**, 2133–2143 (1999).

[26] A. E. Schach von Wittenau, L. J. Cox, P. M. Bergstrom, W. P. Chandler, C. L. H. Siantar, and R. Mohan, "Correlated histogram representation of Monte Carlo derived medical accelerator photon-output phase space," Med. Phys. **26**, 1196–1211 (1999).

[27] H. H. Liu, T. R. Mackie, and E. C. McCullough, "A dual source photon beam model used in convolution/superposition dose calculations for clinical megavoltage x-ray beams," Med. Phys. **24**, 1960–1974 (1997).

[28] K. V. Laere and W. Mondelaers, "Design of field flattening filters for a high-power bremsstrahlung converter by full Monte Carlo simulation," Radiat. Phys. Chem. **49**, 307–317 (1997).

[29] D. W. O. Rogers, B. A. Faddegon, G. X. Ding, C. M. Ma, J. We, and T. R. Mackie, "BEAM: A Monte Carlo code to simulate radiotherapy treatment units," Med. Phys. **22**, 503–524 (1995).

[30] D. M. J. Lovelock, C. S. Chui, and R. Mohan, "A Monte Carlo model of photon beams used in radiation therapy," Med. Phys. **22**, 1387–1394 (1995).

[31] G. F. Knoll, *Radiation detection and measurement, 3ʳᵈ edition* (Wiley-Interscience, New York, 2000).

[32] P. Dorenbos, J. T. M. de Haas, and C. W. E. van Eijk, "Non-proportionality in the scintillation response and the energy resolution obtainable with scintillation crystals," IEEE Trans. Nucl. Sci. **42**, 2190–2202 (1995).

[33] I. A. Cunningham, "Degradation of the detective quantum efficiency due to a non-unity detector fill factor," Proc. SPIE **3032**, 22–31 (1997).

[34] D. R. Dance, S. A. Lester, G. A. Carlsson, M. Sandborg, and J. Persliden, "The use of carbon fibre material in radiographic cassettes: estimation of the dose and contrast advantages," Brit. J. Radiology **70**, 383–390 (1997).

[35] R. A. Schmidt, H. P. Chan, Y. Kodera, K. Doi, and C. T. Chen, "Evaluation of cassette performance: Physical factors affecting patient exposure and image contrast," Radiology **146**, 801–806 (1983).

[36] A.C. Miller, Jr. and J. L. Cochran, "Optimization of process parameters in high-energy film radiography," in D. O. Thompson and D. E. Chimenti (editors), "Review of Progress in Quantitative Nondestructive Evaluation, Vol. 20A," 499–506 (2001), aIP Conference Proceedings #557.

[37] B. M. C. McCurdy and S. Pistorius, "A two-step algorithm for predicting portal dose images in arbitrary detectors," Med. Phys. **27**, 2109–2116 (2000).

[38] J. Boone, "Parametrized x-ray absorption in diagnostic radiology from Monte Carlo calculations:implications for x-ray detector design," Med. Phys. **19**, 1467–1473 (1991).

[39] H. H. Barrett and W. Swindell, *Radiological imaging* (Academic Press, San Diego, 1981).

[40] R. K. Swank, "Absorption and noise in x-ray phosphors," J. Appl. Phys. **44**, 4199–4203 (1973).

[41] F. Jamet and G. Thomer, *Flash Radiography* (Elsevier, Amsterdam, 1976).

[42] M. Frigo and S. G. Johnson, "FFTW: An adaptive software architecture for the FFT," in "Proceedings of the 1998 IEEE International Conference on Acoustics, Speech, and Signal Processing," volume 3, 1381–1384 (1998).

[43] R. Sjögren and M. Karlsson, "Electron contamination in clinical high energy photon beams," Med. Phys. **23**, 1873–1881 (1996).

[44] X. A. Li and D. W. O. Rogers, "Reducing electron contamination for photon beam-quality specification," Med. Phys. **21**, 791–797 (1994).

[45] G. Krithivas and S. N. Rao, "A study of the characteristics of radiation contaminants within a clinically useful beam," Med. Phys. **12**, 764–768 (1985).

[46] P. J. Biggs and M. D. Russell, "An investigation into the presence of secondary electrons in megavoltage photon beams," Phys. Med. Biol. **28**, 1033–1043 (1983).

[47] K. Doi, G. Holje, L. N. Loo, H. P. Chan, J. M. Sandrik, R. J. Jennings, and R. F. Wagner, "MTFs and Wiener spectra of radiographic screen-film systems," Technical Report FDA 82-8187, U.S. Food and Drug Administration (1982).

[48] L. M. Smith, D. R. Keefer, and S. I. Sudharsanan, "Abel inversion using transform techniques," J. Quant. Spectros. Radiat. Transfer **39**, 367–373 (1988).

[49] E. W. Marchand, "Derivation of the point spread function from the line spread function," J. Opt. Soc. Am. **54**, 915–919 (1964).

TABLE I. Photon sources within the radiography facility, calculated at the center of the detector plane, by percent of total.

	Assumed detector sensitivity to photons		
Component	independent of photon energy	proportional to photon energy	calculated flat panel energy sensitivity
Bremsstrahlung target	98.1	98.6	97.0
Primary Collimator	1.5	1.2	1.7
Pb collimators and supporting framework	0.1	0.1	0.2
Walls, ceiling, floor	0.1	0.0	0.7
Air	0.2	0.1	0.4

TABLE II. Materials, densities, and layer thicknesses used for the MCNP simulations of the notional imaging system.

item	material	density (g/cc)	thickness (mm)	areal density (g/cm^2)	integrated areal density (g/cm^2)	% of total integrated areal density
front cover	Carbon fiber sheet	1.6	1.5	0.24	0.24	9.2
air gap	air	0.0012	6.5	0.00078	0.241	9.2
Gd$_2$O$_2$S screen						
protective coating	cellulose acetate	1.32	0.01	0.00132	0.242	9.3
plastic substrate	poly(ethylene terephthalate)	1.38	0.178	0.0246	0.267	10.2
scintillator	Gd$_2$O$_2$S + urethane binder	4.25	0.084	0.0357	0.302	11.6
protective coating	cellulose acetate	1.32	0.005	0.00066	0.303	11.6
electronics						
glass substrate	Corning 1737	2.54	1.1	0.2794	0.582	22.3
plastic sheet	polypropylene	0.988	0.457	0.0452	0.628	24.0
support plate	aluminum 6061	2.7	4.83	1.304	1.932	73.9
air gap	air	0.0012	20.3	0.00244	1.934	74.0
back cover	aluminum 5052	2.68	2.54	0.681	2.615	100.0
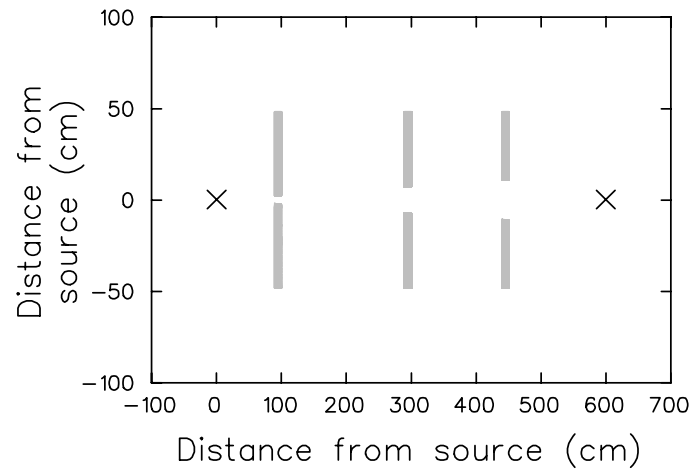
FIG. 1. Schematic of the radiation facility. The source-to-detector distance is 600 cm. There are three Pb collimators with tapered apertures focussed to the source position.
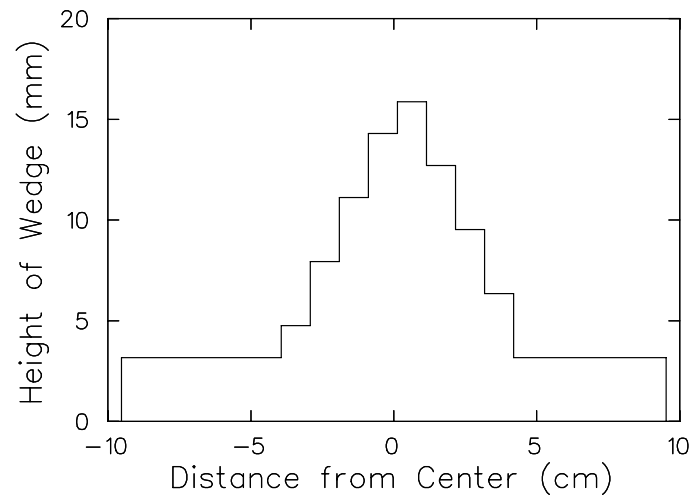
FIG. 2. Cross section of the Cu step wedges.
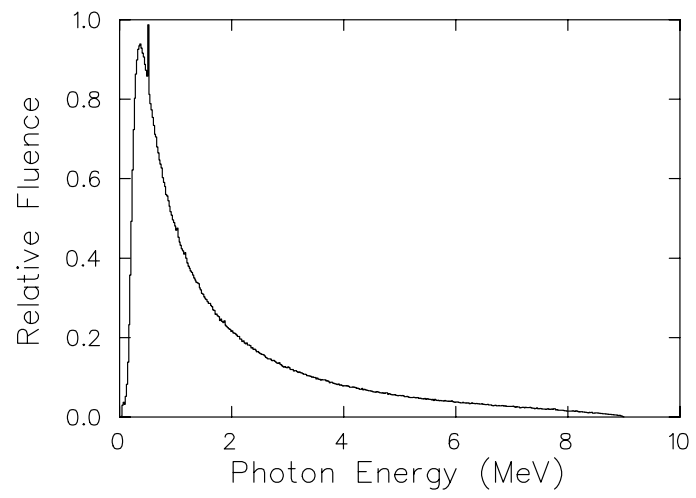
FIG. 3. Photon spectrum of 9 MV linac, as given by MCNP4C simulations.
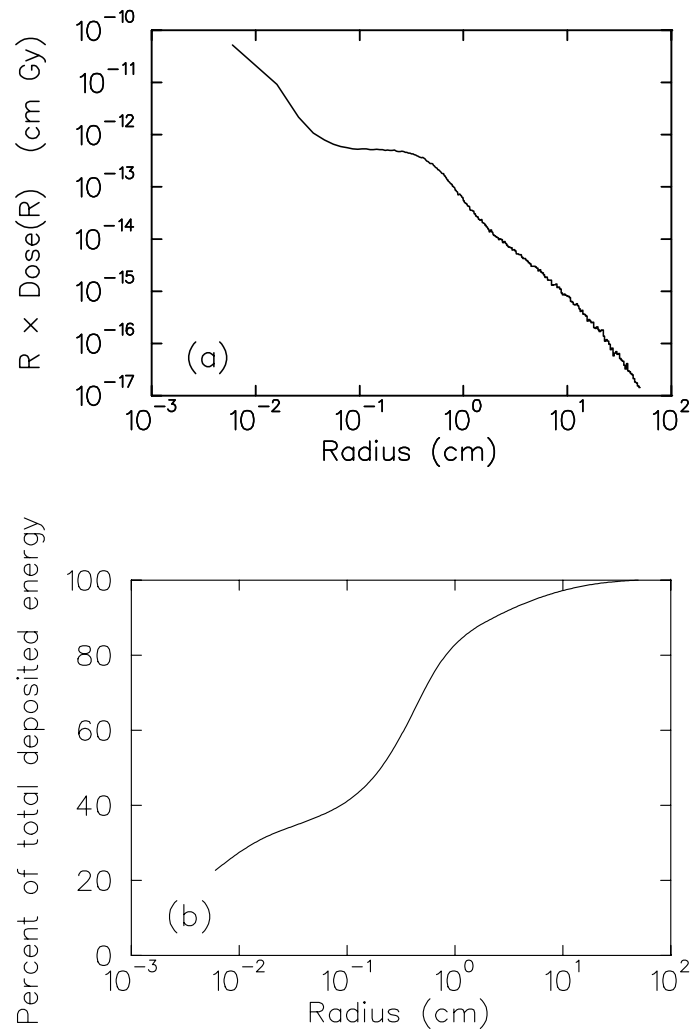
FIG. 4. Radial distribution of energy deposited in the scintillator layer, assuming a 9 MV incident bremsstrahlung spectrum. (a): energy deposition, as tallied. (b): Running integral of the curve in (a), normalized to unity.
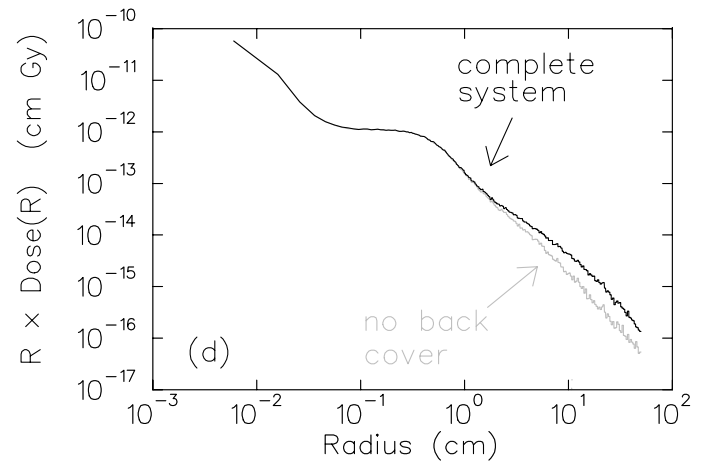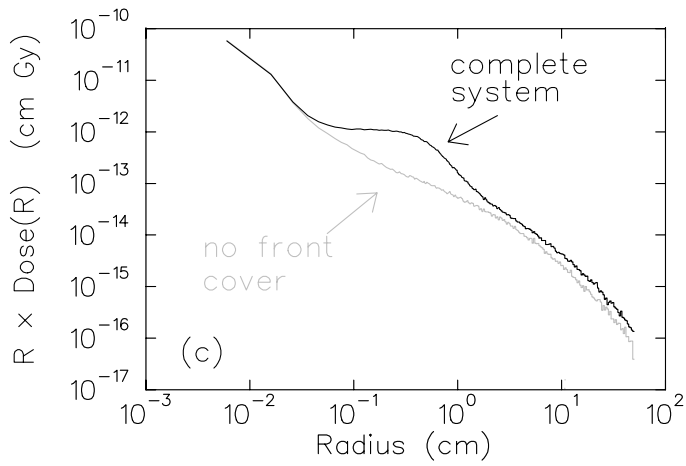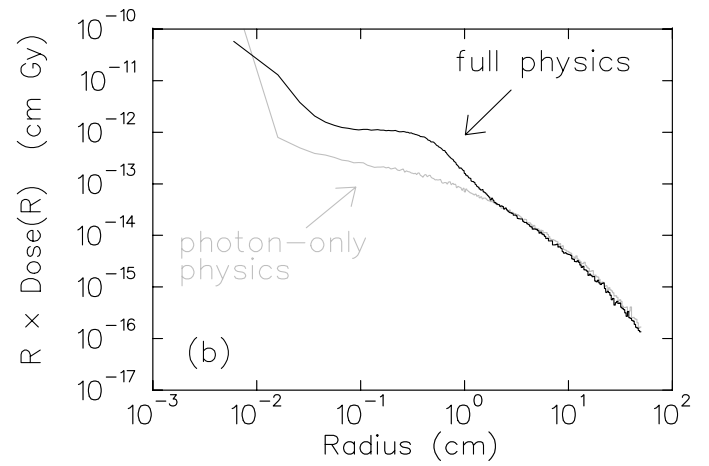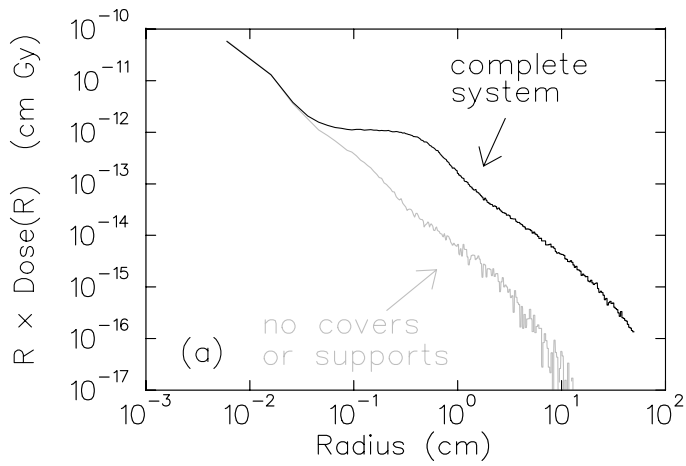
FIG. 5. Radial distribution of energy deposited in the scintillator layer, with various physics processes disabled. (a) photon and electron transport enabled only in the scintillating screen and in the glass substrate. (b) no electron transport anywhere in the detector. (c) electron transport disabled in the front cover and in the first air gap. (d) photon and electron transport disabled in the back cover of the detector.
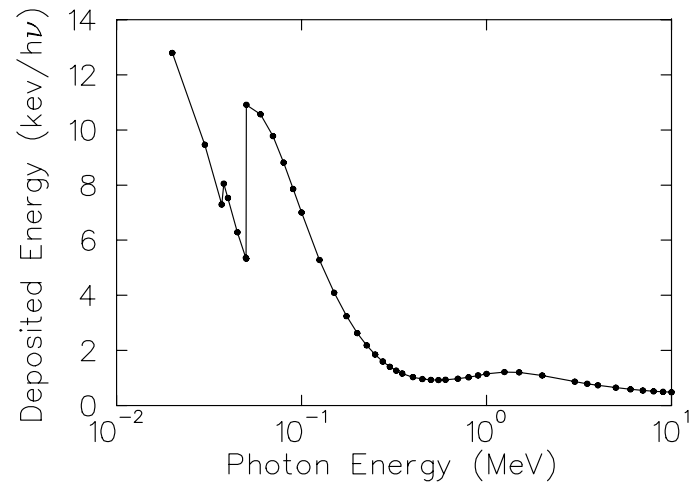
FIG. 6. Average energy deposition in the scintillator layer of the notional detector, per incident photon.
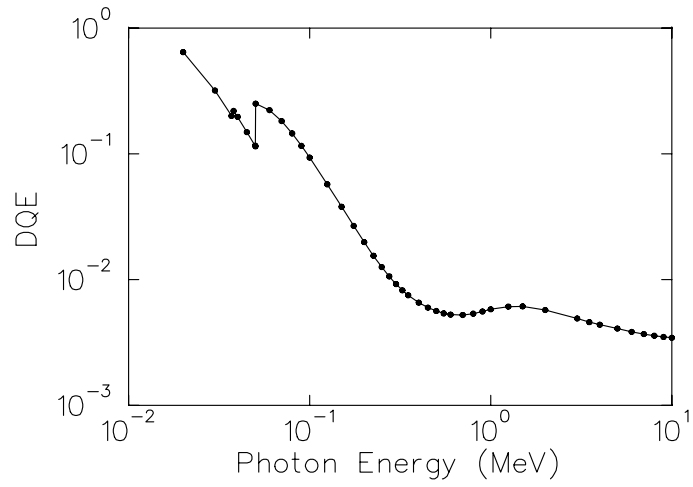
FIG. 7. DQE for energy deposition in the scintillator layer of the notional detector.
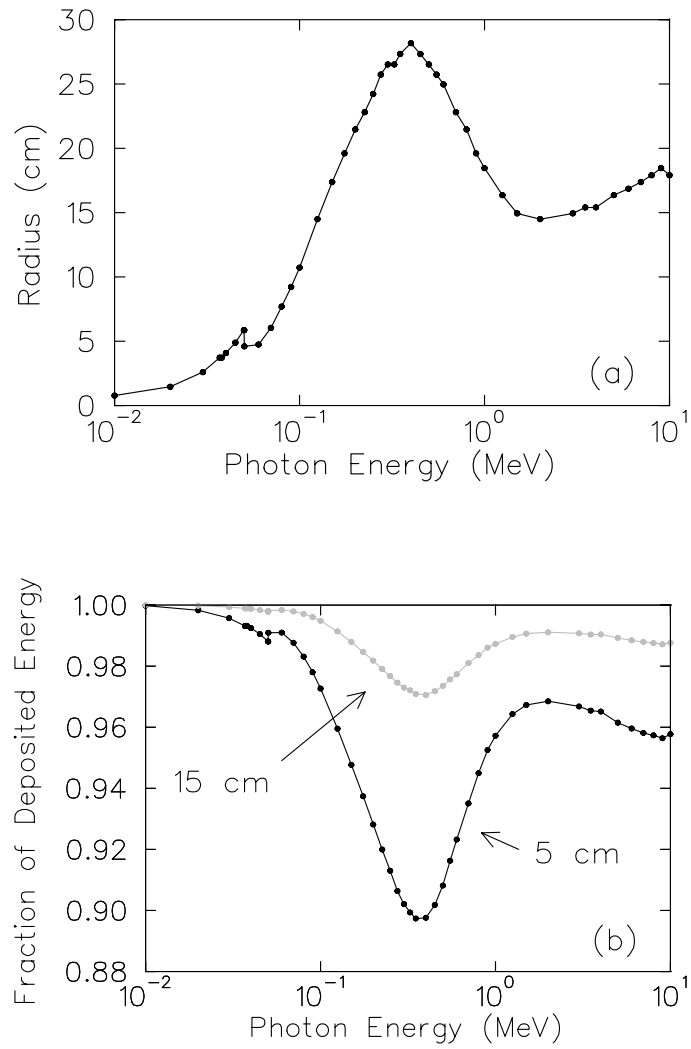
FIG. 8. Radial extent of the energy deposition in the scintillator layer, where the outer radius of the geometry was 50 cm. (a) Radius required to contain 99% of the total energy deposited. (b) Fraction of total energy deposited within the scintillator layer, within a radius of of 5 cm and 15 cm.
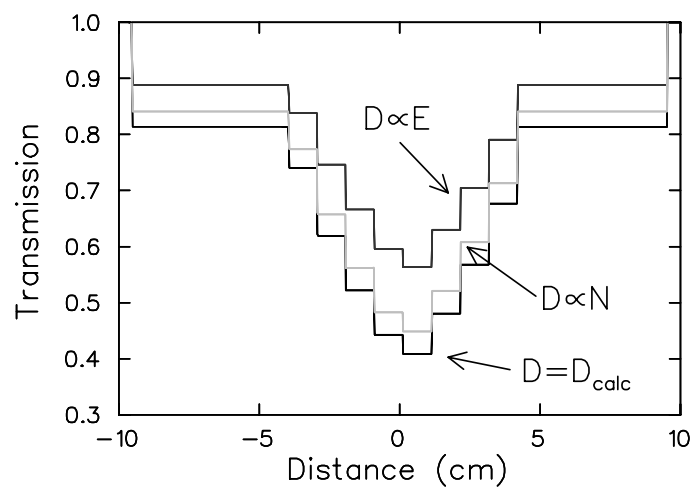
FIG. 9. Apparent transmissivity of Cu step wedge for three different assumed detector response functions.
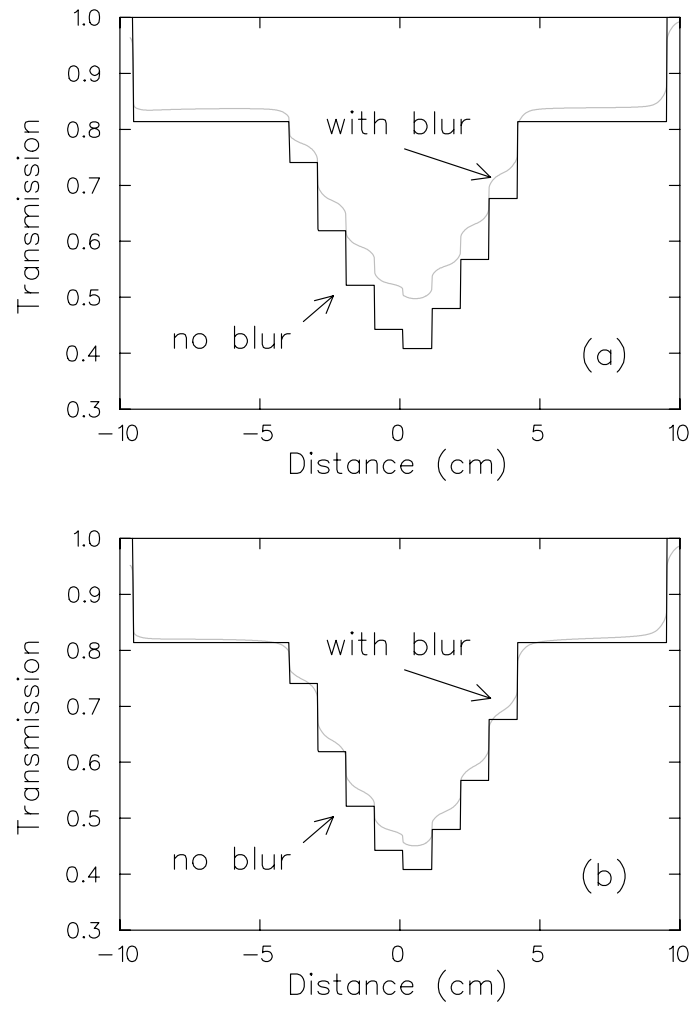
FIG. 10. Effects of blur on apparent transmission. (a) 1.27 cm wide wedge. (b) 5.08 cm wide wedge.
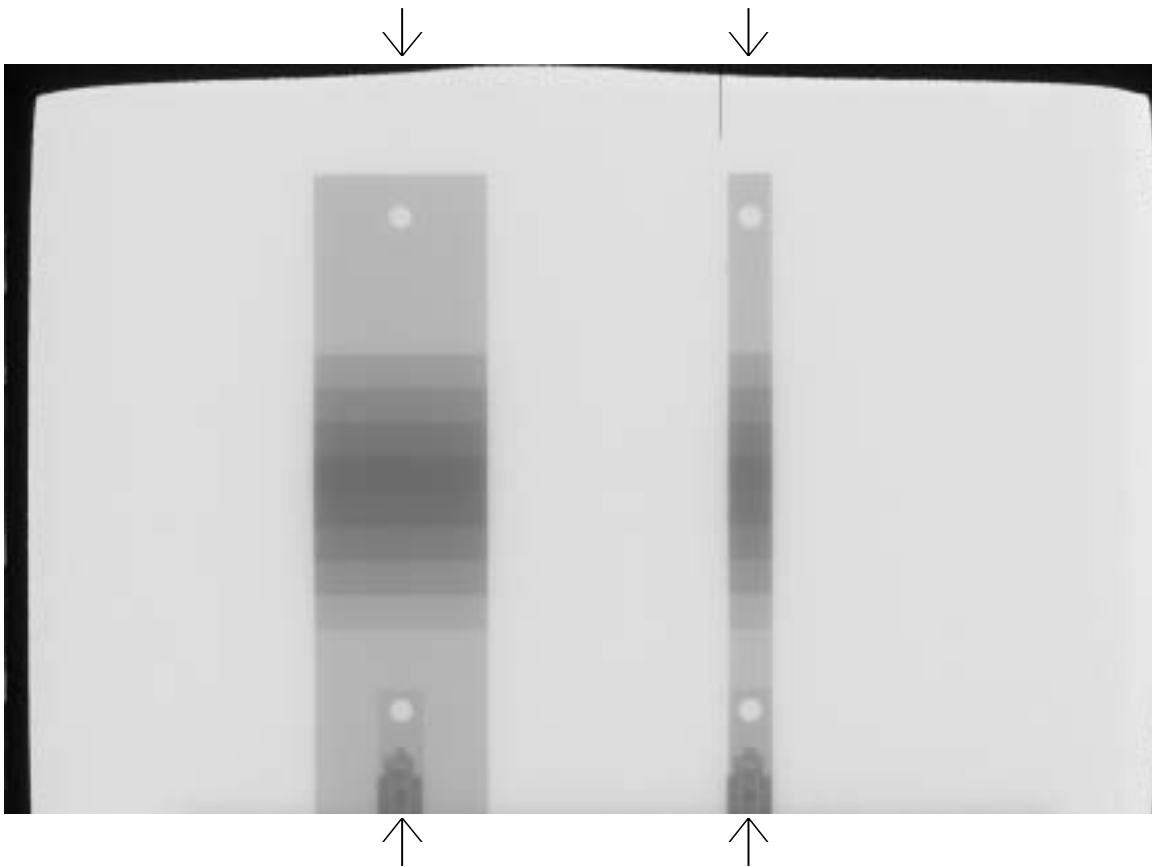
FIG. 11. Radiograph of Cu step wedges. The arrows denote the positions through which the lineouts of Fig. 12 were taken.
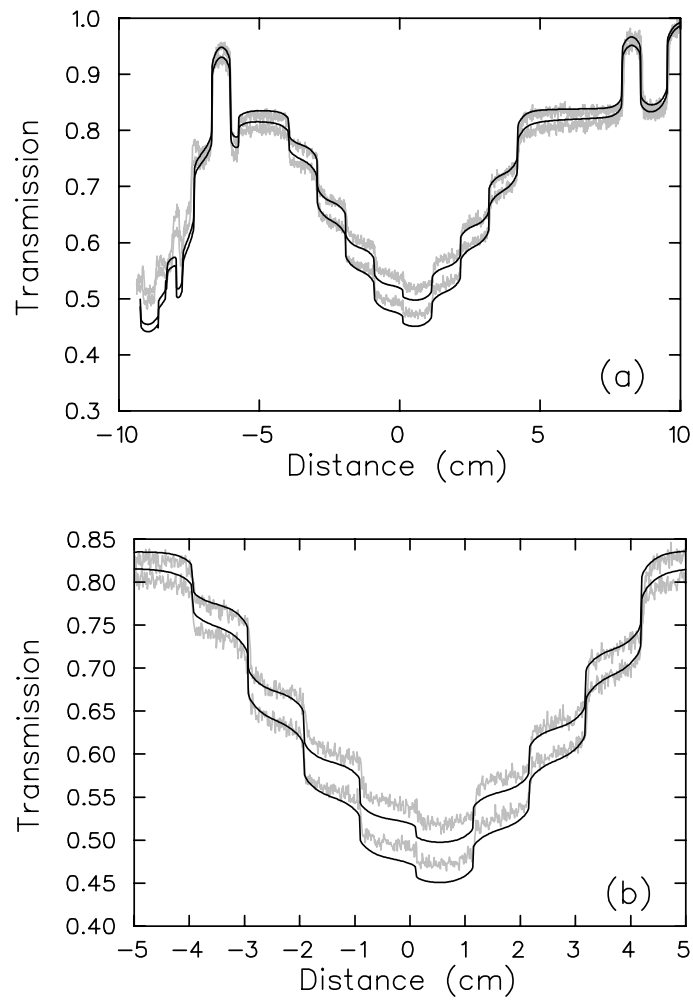
FIG. 12. (a) Lineouts through the wedges in the image shown in Fig. 11, compared with predicted lineouts. (b) The central portion of (a).

Appendix 2

Nine Megavolt Linac Radiography in Pantex Bay 19: Scatter from Collimators and Environment, Schach von Wittenau and Logan, UCRL-ID-146128.

Nine megavolt linac radiography in Pantex Bay 19: Scatter from collimators and environment

Alexis Schach von Wittenau and Clint Logan
Lawrence Livermore National Laboratory
UCID-146128
October 22, 2001

Background

Fielding a prototype High-Energy, High-Resolution CT Scanner at Pantex requires design and installation of a large collimator capable of stopping 9-MV bremsstrahlung x–rays. LLNL has a working collimation system; called Stonehenge II, but some modifications may be needed to accommodate Pantex programmatic requirements. At Pantex request and sponsorship, we used the Monte Carlo code MCNP[1] to evaluate the effect of several potential design modifications. In the course of this study, additional questions arose regarding possible modifications to and effects of misalignment of Stonehenge II at LLNL. We addressed these questions and the results are presented here.

We could do this study quickly and at low cost because we had earlier built a computational model[2, 3] of LLNL Building 239, Rm. B-11 and Stonehenge II.
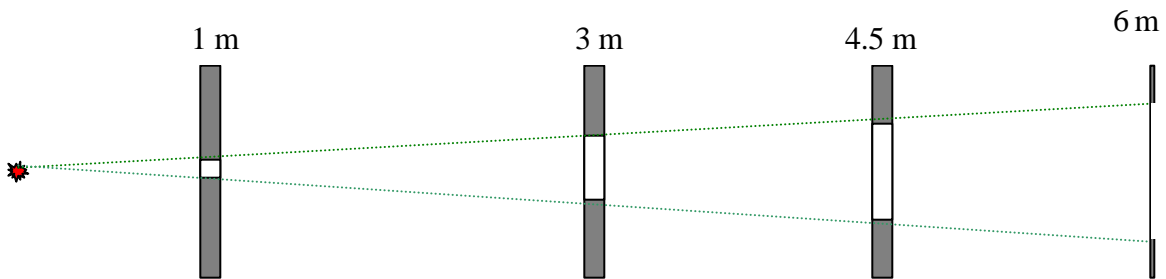

Figure 1   Schematic of the major components of Stonehenge II. The plates at 1.0, 3.0 m and 4.5 m have tapered rectangular openings in 101-mm thick Pb. The Pb plate at 6.0 m is just upstream of the detector position and is 12-mm thick with a tapered opening to match the Varian flat panel imaging area.

For convenience in presenting results we assign the following names to the specified configurations.

StnHngII	LLNL Stonehenge II configuration.
ClsWall	as StnHngII but with one concrete side wall moved to a distance of 1.5 m from centerline.
ThnPb	as ClsWall but with 101-mm Pb plates reduced to 51-mm thickness.
VthnPb	as ClsWall but with 101-mm Pb plates reduced to 26-mm thickness.
ThkPb	as StnHngII but with the Pb collimator 1 m from the source increased to 152-mm thickness.
MissLine	as StnHngII but with the middle collimator plate shifted 2 mm both vertically and horizontally.
Jaws	As ClsWall but with four 38-mm thick W plates with square edges added just downstream of the middle collimator. These plates are located in the the manner of common four-jaw collimators. Opening in the W collimator is 50% of the full-beam linear dimension in both directions.

Note that ThnPb, VthnPb and Jaws are extensions of ClsWall, meaning one wall is at 1.5 m from beam centerline for all of these cases.

We computed variables at two locations, one location at the center of the imaging area and another 25 mm outside of the imaging area. This position, denoted "electronics", is centered on the short side of the imaging area and 8 mm behind the final Pb plate and is meant to be representative of where radiation-sensitive electronics may be located. At each location we computed photon flux, energy flux and panel response as well as other details. Panel response is calculated using the energy-dependent response from Reference 2. *Our computations do not have an object nor a panel present, and therefore do not include scattered radiation from these sources.*

Results

We believe the most relevant metric for image degradation at the image center is panel response to scattered x-rays. In Figure 2, we present normalized panel response from three sources for all seven configurations. These data have been normalized to panel response from photons arriving unperturbed from the W/Cu converter in the Linatron 3000. The four scatter sources presented are:

- Stonehenge II   Four Pb plates with their supporting structure.

- Room   Concrete walls, floor and ceiling.

- Air   Air filling the room.

- W-collimator   additional limiting collimator (configuration Jaws only).
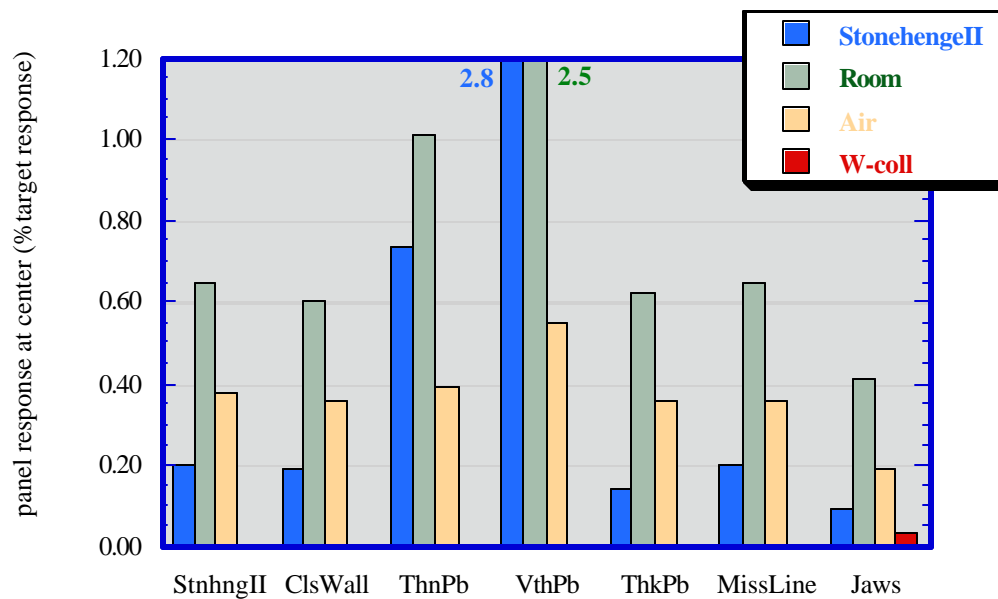

Figure 2   Computed response at center of flat panel imager from four scatter sources and seven configurations. These results are expressed as a percentage of the panel response from photons arriving directly from the W/Cu linac target.

At the electronics position, we believe that the most relevant measure for potential damage to small components is x-ray flux. Accordingly, we present in Figure 3 the x-ray flux at the electronics position as a percentage of the unscattered x-ray flux at the center of the image area.
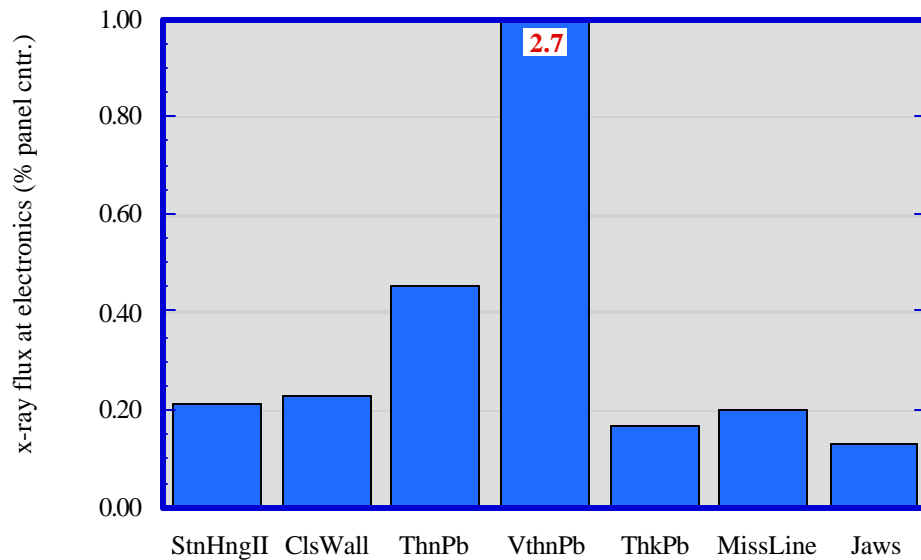
Figure 3   Computed x-ray flux at the electronics position for seven configurations. These results are
            expressed as a percentage of the x-ray flux at the center of the panel from the W/Cu linac
            target. These results are not well converged, meaning that they should be considered
            generally suggestive, but not exact. Configuration VthnPb is off scale.

There is one other top-level result from these calculations. The conical collimator within the
linac is a significant contributor to scatter arriving at the detector. At image center, scatter
(normalized as described previously) from this collimator is 1.53 % of the x-ray flux, 1.24 % of
the energy flux, and 1.76 % of the panel signal.

Turning now to the rich details, we tallied separately within these calculations scatter arising
from each of three component parts of the linac, the W target, the Cu backing and the conical
collimator. If we take the sum of these three as arising from the linac (and for now, out of our
control), we can look at changes from configurations alone, expressing each metric as
linac/total. A perfect design of room and collimation would result in 100% of the each metric
arising from the linac. We present these data for image center in Figure 4.

We next examine the sources of the scatter for each configuration. Scattered x-ray flux is
shown in Figure 5. Scattered energy flux is shown in Figure 6 and panel response to scattered
x-rays is shown in Figure 7. In these figures, StonehengeII denotes the four Pb plates and all
their support structure. Room denotes concrete walls, floor and ceiling and air denotes the air
within the room.
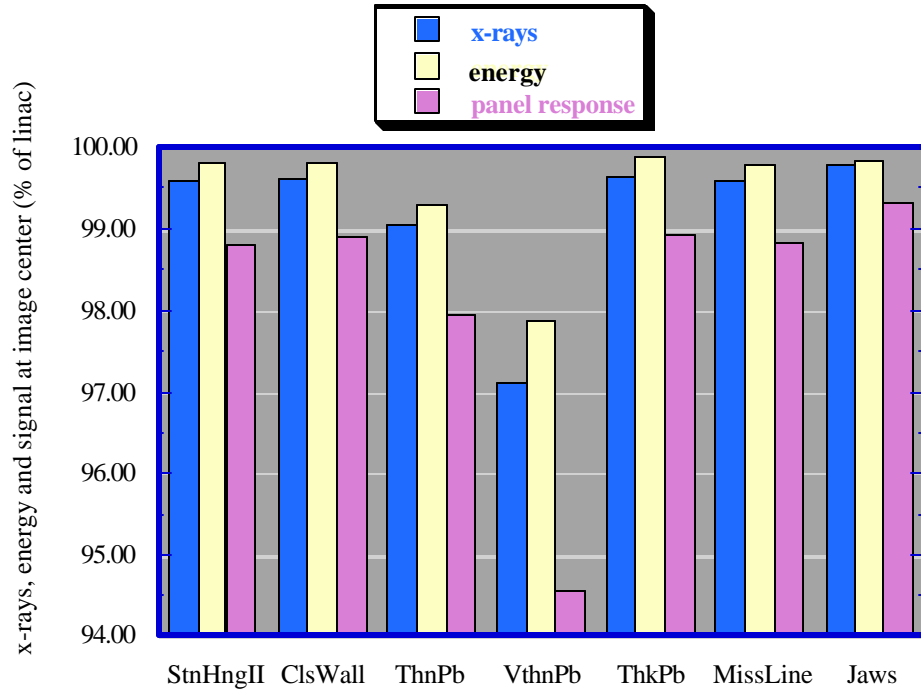
Figure 4   The three metrics at image center expressed as a percent of each metric arising from the linac including Cu backing and primary internal collimator.
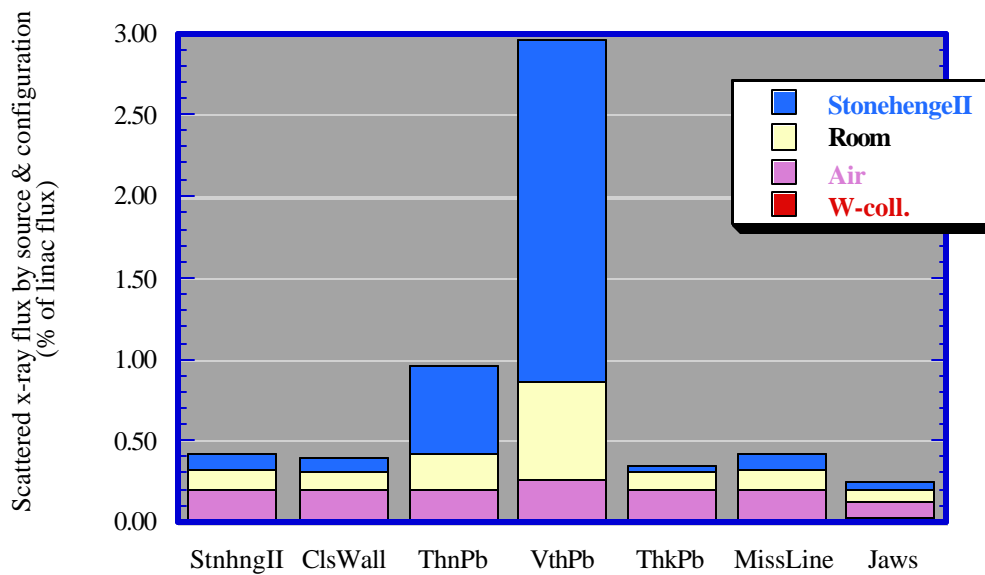

Figure 5   Sources of scattered x-rays at the image center as a percentage of those from linac for all seven configurations.
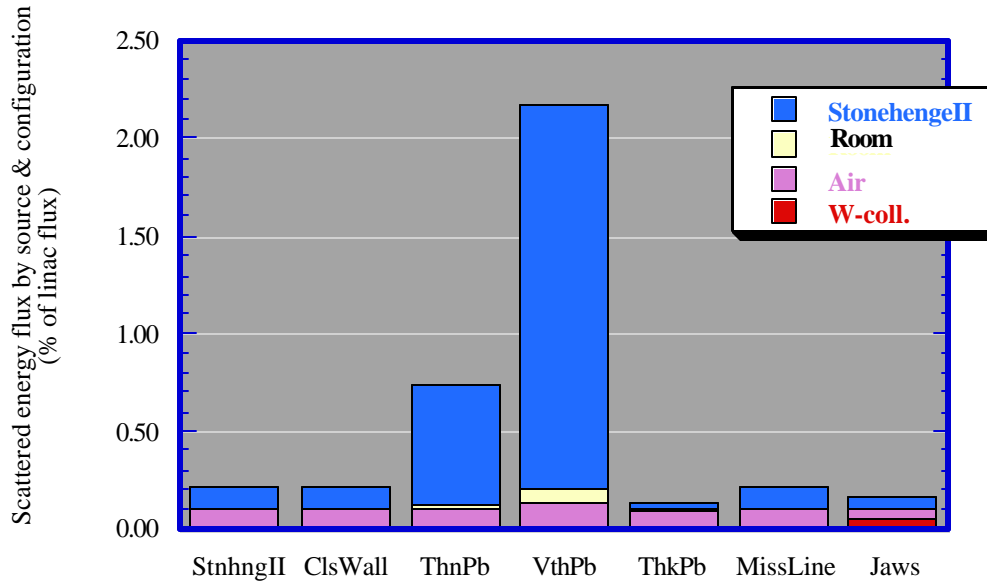
Figure 6   Sources of scattered x-ray energy flux at the image center as a percentage of that from linac for all seven configurations.
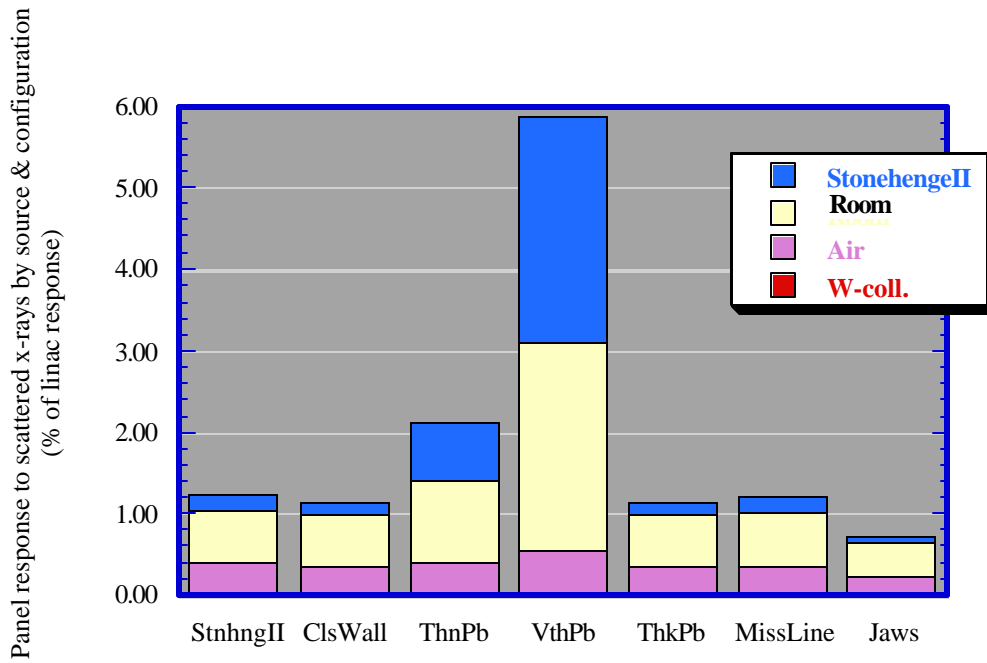

Figure 7   Sources of panel response to scattered x-rays at the image center as a percentage of that from linac for all seven configurations.

Data from which Figures 2-7 are derived are presented in Appendices A & B.

As we were wrapping this report up, we were asked the effect of moving the W jaws to the 5.0-m position. We ran this case. The scatter contribution from the W jaws increases by an order of magnitude compared to the near-3-m position. Scatter from all sources increases though only to a level comparable to the bare StonehengeII configuration. Locating jaws at 5.0 m degrades performance and quadruples cost compared to the middle location. Numbers are presented in Appendix C.

Conclusions

The LLNL Stonehenge II design is (even in hindsight) pretty good. Thickening the collimator at 1-m distance from the source offers negligible benefit and the system is fairly robust to misalignment of the central Pb plate.

Moving one concrete wall so that the centerline is 1.5 m away causes no loss in performance.

Even with more than a foot of Pb between source and the "electronics" position, the x–ray flux is still 0.2 % of that at the center of the imaging area. This is consistent with dosimetry done separately by LLNL and suggests a dose rate of 7 ± 4 R/hr at this location without considering scattered radiation from panel and object.

Thinning the 101-mm Pb plates to 51 mm or less is not acceptable.

Adding a 38-mm thick W collimator just downstream of the central Pb plate slightly improves overall collimation performance. Note that this is not a replacement, but an addition. While we tested only one opening, cutting the beam to 25 % area, we expect this would be the case for any opening. In addition, reducing the active imaging area will significantly decrease *detector* scatter effects[2] for flat panel imagers of current design. For objects requiring less than the full detector area, additional collimation at the central location is highly desirable.

Adding a 38-mm thick W collimator at the 5.0-m position degrades performance compared to downstream of the central Pb plate.

As shown in Figures 5, 6 and 7, excluding the unacceptable thin-Pb-plate configurations, the ranking of scatter sources is: 1) room, 2) air, and 3) StonehengeII. We suspect from other work[3] (but did not evaluate here) that the major source of room scatter is the back wall.

Future work on higher output linacs should pay attention to potential reduction in the scatter from the internal primary collimator.

References

1. J. F. Briesmeister, "MCNP — A general Monte Carlo n‑particle transport code," Technical report LA‑13709‑M, Los Alamos National Laboratory (2000).

2. A.E. Schach von Wittenau, C. M. Logan, M. B. Aufderheide and D. M. Slone, *"Blurring Artifacts in Megavoltage Radiography with a Flat‑Panel Imaging System: Comparison of Monte Carlo Simulations with Measurements"*, Submitted to Medical Physics. UCRL‑JC‑144247 (2001).

3. C. M. Logan and A. E. Schach von Wittenau, *"Effects of Backshield Albedo on Imagery with a dpiX Flashscan20 Using a 9-MV Bremsstrahlung Spectrum,"* Materials Evaluation **59:5**, 617-20 (2001).

Appendix A

Flux

	target	backing	primary collimator	total	electronics
1) photons					
StnHngII	3.238E-06	8.544E-08	5.094E-08	3.388E-06	6.797E-09
ClsWall	3.239E-06	8.540E-08	5.098E-08	3.388E-06	7.453E-09
ThnPb	3.238E-06	8.544E-08	5.099E-08	3.407E-06	1.444E-08
VthnPb	3.237E-06	8.545E-08	5.121E-08	3.473E-06	8.933E-08
ThkPb	3.238E-06	8.543E-08	5.076E-08	3.386E-06	5.514E-09
MissLine	3.238E-06	8.551E-08	5.093E-08	3.389E-06	6.426E-09
Jaws	3.239E-06	8.550E-08	5.096E-08	3.384E-06	4.140E-09
2) energy					
StnHngII	6.177E-06	6.446E-08	7.722E-08	6.332E-06	5.448E-09
ClsWall	6.181E-06	6.445E-08	7.725E-08	6.335E-06	3.991E-09
ThnPb	6.178E-06	6.443E-08	7.734E-08	6.366E-06	1.707E-08
VthnPb	6.176E-06	6.445E-08	7.769E-08	6.455E-06	1.755E-07
ThkPb	6.179E-06	6.447E-08	7.699E-08	6.329E-06	2.382E-09
MissLine	6.181E-06	6.456E-08	7.713E-08	6.336E-06	3.914E-09
Jaws	6.179E-06	6.445E-08	7.721E-08	6.330E-06	3.391E-09
3) panel response					
StnHngII	3.426E-09	1.464E-10	6.301E-11	3.680E-09	2.750E-11
ClsWall	3.427E-09	1.464E-10	6.304E-11	3.677E-09	3.635E-11
ThnPb	3.426E-09	1.466E-10	6.303E-11	3.712E-09	4.252E-11
VthnPb	3.425E-09	1.466E-10	6.324E-11	3.844E-09	1.611E-10
ThkPb	3.426E-09	1.468E-10	6.278E-11	3.676E-09	2.670E-11
MissLine	3.427E-09	1.466E-10	6.291E-11	3.679E-09	2.927E-11
Jaws	3.427E-09	1.467E-10	6.305E-11	3.663E-09	1.974E-11

The units are:

1) photons per cm^2, per electron incident on the linac bremsstrahlung target.

2) MeV per cm^2, per electron incident on the linac bremsstrahlung target.

3) MeV deposited in scintillating layer per cm^2, per electron incident on the linac bremsstrahlung target.

The columns are:

Target refers only to the W converter.

Backing refers to the Cu backing of the converter.

Primary collimator refers to the fixed conical collimator internal to the linac.

Total is the total flux from all sources.

Electronics is the flux at the position defined as electronics. (see text of report)

Appendix B
Normalized flux at panel center by configuration and source.

Configuration	Photons	energy	pan. response
StnhngII			
Target	100.00	100.00	100.00
Primary Collimator	1.53	1.24	1.76
Fixed Collimator Structure	0.10	0.10	0.20
Room	0.13	0.01	0.65
Air	0.19	0.10	0.38
ClsWall			
Target	100.00	100.00	100.00
Primary Collimator	1.53	1.24	1.76
Fixed Collimator Structure	0.09	0.10	0.19
Room	0.12	0.01	0.60
Air	0.19	0.10	0.36
ThnPb			
Target	100.00	100.00	100.00
Primary Collimator	1.53	1.24	1.76
Fixed Collimator Structure	0.55	0.62	0.73
Room	0.23	0.02	1.01
Air	0.20	0.10	0.39
VthPb			
Target	100.00	100.00	100.00
Primary Collimator	1.54	1.25	1.77
Fixed Collimator Structure	2.12	2.00	2.76
Room	0.62	0.07	2.54
Air	0.26	0.13	0.55
ThkPb			
Target	100.00	100.00	100.00
Primary Collimator	1.53	1.23	1.76
Fixed Collimator Structure	0.04	0.03	0.14
Room	0.12	0.01	0.62
Air	0.19	0.09	0.36
MissLine			
Target	100.00	100.00	100.00
Primary Collimator	1.53	1.24	1.76
Fixed Collimator Structure	0.10	0.10	0.20
Room	0.13	0.01	0.65
Air	0.19	0.10	0.36
Jaws			
Target	100.00	100.00	100.00
Primary Collimator	1.53	1.24	1.76
Fixed Collimator Structure	0.04	0.05	0.09
Room	0.08	0.01	0.41
Air	0.09	0.05	0.19
W - collimator	0.03	0.05	0.03

Target denotes the W converter and its Cu backing.

Primary Collimator denotes the fixed conical collimator internal to the linac.

Stonehenge II denotes the four Pb plates of Stonehenge II with their supporting structure.

Room denotes concrete walls floor and ceiling.

Air denotes the air filling the room.

W-collimator denotes an additional limiting collimator (configuration Jaws only).

Appendix C
Normalized flux at panel center by configuration and source:
Comparison of two jaws locations

	Jaws near 3 m				Jaws at 5.0 m		
	photons	energy	pan. rsp.		photons	energy	pan. rsp.
Target	100.00	100.00	100.00		100.00	100.00	100.00
Primary Collimator	1.53	1.24	1.76		1.53	1.24	1.76
Fixed Collimator Structure	0.04	0.05	0.09		0.09	0.10	0.16
Room	0.08	0.01	0.41		0.10	0.01	0.50
Air	0.09	0.05	0.19		0.13	0.07	0.26
W - collimator	0.03	0.05	0.03		0.22	0.28	0.20

University of California
Lawrence Livermore National Laboratory
Technical Information Department
Livermore, CA. 94551